

Constraining the Interiors of Asteroids Through Close Encounters

Jack T. Dinsmore,^{1*} Julien de Wit²

¹*Department of Physics, Massachusetts Institute of Technology*

²*Department of Earth, Atmospheric, and Planetary Science, Massachusetts Institute of Technology*

Accepted XXX. Received YYY; in original form ZZZ

ABSTRACT

Knowledge of the interior density distribution of an asteroid can reveal its composition and constrain its evolutionary history. However, most asteroid observational techniques are not sensitive to interior properties. We investigate the interior constraints accessible through monitoring variations in angular velocity during a close encounter. We derive the equations of motion for a rigid asteroid’s orientation and angular velocity to arbitrary order and use them to generate synthetic angular velocity data for a representative asteroid on a close Earth encounter. Using Markov Chain Monte Carlo fits, we perform injection-retrieval tests on these synthetic data to gain insights into the extent to which interior properties can be constrained. We also perform a sensitivity analysis of such an inversion technique to asteroid parameters (e.g., moment of inertia and initial spin pole direction), observational set-up (e.g., measurement precision and cadence), and mapping models to convert constraints on the density moments to density distributions. We find that high precision in rotational period estimates (order of milliseconds to seconds) are necessary for each cadence, and that large asteroids (> 100 m radius) with low perigees (< 20 Earth radii) are necessary to resolve second-order density moments.

Key words: minor planets, asteroids: general – methods: data analysis

1 INTRODUCTION

Over the past twenty years, the increase in quantity and quality of sensitive all-sky surveys has prompted the discovery of numerous asteroids. Such advances have been made via ground-based surveys such as the Catalina Sky Survey [Larson et al. \(1998\)](#), Pan-STARRS [Kaiser et al. \(2002\)](#), and the Lincoln Near-Earth Asteroid Research project (LINEAR) [Stokes et al. \(2000\)](#), as well as space-based instruments such as the Wide-field Infrared Survey Explorer (WISE) mission [Wright et al. \(2010\)](#). Many of these asteroids are relatively small, but some are kilometre-sized and a few are predicted to closely encounter Earth or other planets in the near future. More encounter candidates are likely to be discovered by new efforts such as the Large-aperture Synoptic Survey Telescope (LSST) [Tyson \(2002\)](#). Their encounters can then be monitored by global ground-based networks such as the Las Cumbres Observatory (LCO) [Brown et al. \(2013\)](#). Such ground-based monitoring is typically used to derive the rotation period of an asteroid and its surface properties (see e.g. [Devogèle et al. \(2021\)](#)).

Since the tidal torque acting on an asteroid during an

encounter depends on the interior mass distribution, the careful monitoring of angular velocity variations during an encounter also presents a window into the interior properties of asteroids. The gravitational two-body system has been studied in the context of tidal torque to different orders and with several different methods [Paul \(1988\)](#); [Scheeres et al. \(2000\)](#); [Ashenbergs \(2007\)](#); [Boué & Laskar \(2009\)](#); [Hou et al. \(2017\)](#). Further studies showed that the tidal torque, observed through angular velocity perturbations, is sensitive to asteroid interior density distribution [Naidu & Margot \(2015\)](#); [Makarov et al. \(2022\)](#); [Scheeres et al. \(2004\)](#). However, density distribution features beyond the moment of inertia ratios have not yet been extracted for any asteroid encounters. More research is needed to study in what cases these effects are observable, and what factors generally inhibit observation of these new features.

Angular velocity perturbations have been observed and used to extract asteroid properties in several cases, including for the 2013 encounter of (367943) Duende with Earth [Moskovitz et al. \(2020\)](#); [Benson et al. \(2020\)](#), and asteroid binaries (3905) Doppler and (617) Patroclus [Descamps et al. \(2020\)](#); [Berthier et al. \(2020\)](#). Orbital and physical properties, including moment of inertia ratios have also been extracted for 99942 Apophis, which will closely encounter

* E-mail: jtdinsmo@mit.edu

Earth in 2029 Yu et al. (2014); Hirabayashi et al. (2021); Valvano et al. (2022); Lee et al. (2022). It seems pivotal to augment previous work on the affect of tidal torque on Apophis’ angular velocity Souchay et al. (2014, 2018) so that upcoming observations may constrain these properties and thus improve our predictions.

We address this community need by developing a methodology to translate (1) time series of asteroid angular velocity data into constraints on density moments and (2) constraints on density moments into constraints on an asteroid’s density distribution. Other techniques, such as measurement of tidal distortion Richardson et al. (1998), impact or seismometry experiments Richardson et al. (2005), or gradiometry Carroll & Faber (2018), may additionally constrain the density distribution. In section 2, we introduce the analytical and numerical fundamentals of this methodology. There, we describe a simulation used to integrate the equations of motion and produce synthetic data of angular velocity over time, followed by a Markov Chain Monte Carlo (MCMC) fit process which extracts density moments from the fit data. We note that these equations of motion for an asteroid equation are novel and designed to be computationally efficient and valid to arbitrary order. We then describe three methods to generate full density distributions from the density moments. In section 3, we present the results of a series of injection-retrieval tests demonstrating the extent to which the properties of an asteroid chosen to generate synthetic spin data can be retrieved via our methodology. Finally, in section 4, we assess the sensitivity of these constraints to various physical, observational, and methodological parameters to provide guidance for monitoring upcoming close encounters. We also test the density distribution extraction methods on several sample asteroids.

2 METHODS

The only properties of an asteroid’s density moments that affect tidal torque interactions are its “density moments,” defined here as

$$K_{\ell m} = \frac{1}{\mu_A a_{\text{bulk}}^2 a_{\text{surf}}^{\ell-2}} \int_{\mathcal{A}} d^3 r \rho_A(\mathbf{r}) R_{\ell m}(\mathbf{r}). \quad (1)$$

These are complex, unitless quantities. $\rho_A(\mathbf{r})$ is the asteroid density distribution, μ_A is the asteroid mass, and $R_{\ell m}$ are the regular solid spherical harmonics (see appendix A for details). The integral is computed over the entire asteroid mass, denoted \mathcal{A} . The two length scales a_{surf} and a_{bulk} are defined as

$$a_{\text{bulk}}^2 = \frac{1}{\mu_A} \int_{\mathcal{A}} d^3 r \rho_A(\mathbf{r}) r^2 \quad a_{\text{surf}}^2 = \frac{1}{V_A} \int_{\mathcal{A}} d^3 r r^2 \quad (2)$$

where V_A is the asteroid volume. We highlight two crucial details of these length scales: (1) that they are equal when ρ_A is uniform across the asteroid, and (2) that a_{surf} is a function only of the boundary of \mathcal{A} whereas a_{bulk} is a function of the internal density distribution.

The tidal torque experienced by an asteroid is

$$\begin{aligned} \tau = & G \frac{\mu_A \mu_B}{2} \left[a_{\text{bulk}}^2 \sum_{\ell m} a_B^\ell J_{\ell m} \sum_{\ell' m'} a_{\text{surf}}^{\ell'-2} S_{\ell+\ell', m+m'}^*(\mathbf{D}) (-1)^{\ell'} \right. \\ & \times \sum_{m''=-\ell'}^{\ell'} \sqrt{\frac{(\ell'-m'')!(\ell'+m'')!}{(\ell'-m')!(\ell'+m')!}} \mathcal{D}_{m'm''}^{\ell'}(\alpha, \beta, \gamma)^* \\ & \times \left. ((i\hat{\mathbf{x}} - \hat{\mathbf{y}})(\ell' - m'' + 1) K_{\ell', m''-1} \right. \\ & \left. + (i\hat{\mathbf{x}} + \hat{\mathbf{y}})(\ell' + m'' + 1) K_{\ell', m''+1} + 2im'' \hat{\mathbf{z}} K_{\ell', m''}) \right], \end{aligned} \quad (3)$$

where \mathbf{D} is the position of the asteroid; α , β , and γ are $z - y - z$ Euler angles expressing the orientation of the asteroid; $S_{\ell m}$ are the irregular solid spherical harmonics; and μ_B and a_B are the mass and radius of the central body while $J_{\ell m}$ are the density moments of the central body, with the a_{bulk} and a_{surf} of equation 1 replaced by a_B . Equation 3 is derived in appendix A, assuming a rigid asteroid and no third-body perturbations.

Since it is the angular acceleration of the asteroid that is observable, rather than the torque applied, we also compute the moment of inertia of the asteroid around the principal axes:

$$\begin{aligned} I_x &= \frac{2}{3} \mu_A a_{\text{bulk}}^2 (K_{20} - 6K_{22} + 1) \\ I_y &= \frac{2}{3} \mu_A a_{\text{bulk}}^2 (K_{20} + 6K_{22} + 1) \\ I_z &= \frac{2}{3} \mu_A a_{\text{bulk}}^2 (-2K_{20} + 1). \end{aligned} \quad (4)$$

The angular acceleration of the asteroid is proportional to τ/I (equation A14), such that the a_{bulk}^2 factor of equation 3 is canceled out. Thus, the observables do not depend explicitly on a_{bulk} .

Throughout the paper, we refer to the “inertial frame” (the frame in which the orbit is fixed) and the “body-fixed frame” (the frame in which the asteroid is fixed), which are also defined in appendix A.

2.1 Simulation design

We built a publicly accessible, custom simulation in C++ to produce time series of angular velocity data during a close encounter with a central body. This simulation requires as initial data (1) the orbital parameters of the asteroid r_p (perigee distance) and v_∞ (hyperbolic excess velocity); (2) the cadence of angular velocity observation Δt ; (3) the central body moments $J_{\ell m}$, mass μ_B , and radius a_B ; (4) the initial asteroid angular velocity in the inertial frame Ω_0 ; (5) the asteroid length a_{surf} and (6) the asteroid’s density moments $K_{\ell m}$ and initial Euler angle γ_0 . All parameters except (6) are assumed to be known to high accuracy. For example, Ω_0 could be extracted from pre-encounter light-curve data and a_{surf} from a model for the asteroid’s surface using radar.

We assume for simplicity that the asteroid is initially not tumbling, though this assumption can be relaxed. We assume a short-axis rotation mode such that energy of the asteroid’s rotation is minimized. This sets $\beta = 0$ and we can further choose $\alpha = 0$. Only the Euler angle γ_0 is necessary to provide initial data for the simulation.

We begin our simulation at $D = 10r_p$, with velocity predicted by Kepler's laws given by the orbital parameters. Since the leading order of the equations of motion is $\ell' = 2, \ell = 0$, this corresponds roughly to a torque of 10^{-3} times the maximum torque at perigee. Unless otherwise indicated, the simulation is terminated at $D = 10r_p$ as well.

With the simulation inputs specified, the equations of motion are integrated via the Runge-Kutta fourth order method, with a variable time step

$$dt = dt_{\min} + 10^{-3}(dt_{\max} - dt_{\min}) \left[\left(\frac{D}{r_p} \right)^3 - 1 \right]. \quad (5)$$

The parameters dt_{\max} and dt_{\min} (20 and 10 seconds respectively) were chosen such that the numerical integration error was ~ 100 times the floating point error, and that neighbouring values of $K_{\ell m}$ yielded significantly different spin pole data compared to floating point error. The data used to choose this dt was obtained using the reference asteroid configuration, described in appendix B.

2.2 Uncertainty model

To add noise to data generated via the above simulation, we use the following uncertainty model. Each asteroid spin vector Ω is assumed to be uncorrelated with other spin vectors, and we model uncertainty in the orientation and in the period as also uncorrelated. Consider a true spin vector Ω^* . For the sake of description, we work in coordinates in which $\Omega^* \parallel \hat{z}$. Then, expressing the observed spin vector Ω in spherical coordinates, we draw the polar angle from a normal distribution with standard deviation σ_θ centred on zero and the azimuthal angle from a uniform distribution. We also draw the ratio $\rho = \Omega/\Omega^*$ from a log-normal distribution centred on one, with width σ_ρ . This width is related to the uncertainty in asteroid period σ_P by $\sigma_P = P\sigma_\rho$ for small σ_ρ . Explicitly, the probability density function (PDF) of ρ is

$$P(\rho) = \frac{1}{\rho\sqrt{2\pi\sigma_\rho^2}} \exp\left(-\frac{\ln^2 \rho}{2\sigma_\rho^2}\right). \quad (6)$$

See figure 1 for an illustration of the uncertainty model. A log normal distribution is chosen such that $\rho > 0$, but since $\sigma_\rho \ll 1$ typically in our analysis, $P(\rho)$ is approximately Gaussian.

The log likelihood resulting from this uncertainty model is (excluding additive constants)

$$\ln \mathcal{L} = -\frac{1}{2} \sum_{i=0} \left[\frac{\cos^{-1}(\Omega_i^* \cdot \Omega_i / (\Omega_i^* \cdot \Omega_i))^2}{\sigma_\theta^2} + \frac{\ln(\Omega_i / \Omega_i^*)^2}{\sigma_\rho^2} + 2 \ln \frac{\Omega_i}{\Omega_i^*} \right]. \quad (7)$$

where Ω_i is the i th spin vector in the data set.

This model was chosen because it separates spin pole and period uncertainty. Therefore, if one is more precisely determined by measurement, σ_θ and σ_ρ can be adjusted separately in accordance.

2.3 Extracting density moments from spin data

Given synthetic data, an Affine Invariant MCMC Ensemble sampler was used to generate PPDs from flat priors. We use

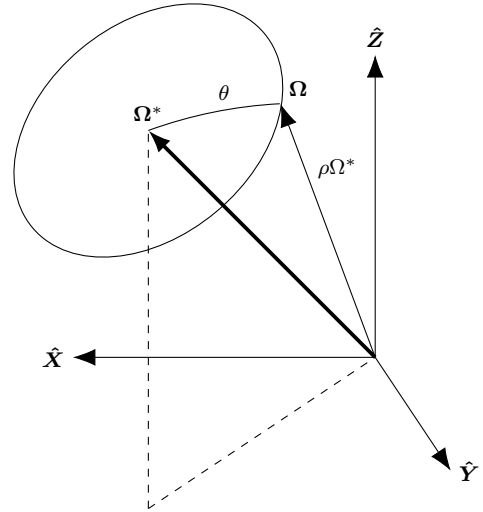


Figure 1. Diagram in the inertial frame of the uncertainty model used to define the probability that the true spin vector Ω^* should be observed as Ω . The parameter θ is drawn from a Gaussian with width σ_θ , and ρ is drawn from a log normal distribution with width σ_ρ .

the Python implementation `emcee` Foreman-Mackey et al. (2013). Our parameters were γ_0 , K_{20} , K_{22} , and K_{3m} (10 in total), and were bounded by $|\gamma_0| < \pi/4$, and bounds on K_{2m} given in equation A5. Note that γ_0 is degenerate with $\gamma_0 + \pi/2$ because both of these align the asteroid principal axes with the body-fixed axes. The other bounds were $|K_{3m}| < 1$. In general, spin data is most sensitive to γ_0 and K_{2m} , which we call the “first-order parameters.” We call K_{3m} the “second-order parameters.”

The MCMC was determined to converge when the fractional change in autocorrelation time (computed every 100 iterations) was one percent, and the number of iterations computed so far was more than 100 times the autocorrelation time. The MCMC fit also was set to terminate if more than 10^5 iterations were run, but this only occurred for fits in which the data quality was low, leading to degeneracies between the second order parameters (K_{3m}). This degeneracy could be removed by only fitting K_{2m} instead. About 10^4 iterations was often sufficient, which generally consumed about 7 hours of computation time on a super computer running 16 threads on 8 cores.

Before the MCMC was run, local minima in the likelihood were found via the Nelder-Mead algorithm implemented in `scipy` Gao & Han (2012). Generally, only one local minimum existed, except when $K_{22} = 0$ in which case rotational symmetry caused multiple values of γ_0 to be degenerate. Ensemble walkers were initialized near this local minimum, distributed by a Gaussian approximation of the likelihood, as determined via the Hessian of the likelihood at the minimum. Due to the high sensitivity of the angular velocity data to density moments, the minimization procedure sometimes failed to isolate the minimum likelihood. Therefore, a simpler simulation without the K_{3m} terms of equation 3 was first used to minimize likelihood as a function of the first-order parameters γ_0 and K_{2m} , and then the full simulation was used to find the second-order parameters K_{3m} with the first-order parameters fixed.

To further ensure convergence, we minimized with respect to data truncated after perigee at double the perigee distance. This cut-off was manually chosen. The minimum was then further refined by minimizing based on the full data, with the previous minimum as the initial estimate.

2.4 Translating constraints on density moments into constraints on the density distribution

The asteroid density distribution $\rho_A(\mathbf{r})$ is not uniquely constrained via tidal torque interactions because only the density moments $K_{\ell m}$ contribute to equation 3. For example, since the mass of the asteroid is unconstrained, $\rho_A(\mathbf{r})$ cannot be determined on an absolute scale. However, by making sufficient assumptions about the density distribution, we can nevertheless extract fluctuations in $\rho_A(\mathbf{r})$ across the asteroid from $K_{\ell m}$.

We assume that the asteroid's surface is known in the inertial frame from radar data. Since the asteroid tumbles during the encounter, we also assume that the center of mass of the asteroid is extracted. However, the density moments which are extracted from flyby data are known in the body-fixed frame.

We rotate the known surface of the asteroid to a new frame called the “hybrid frame” by translating such that the known center of mass is at the origin, then rotating such that Ω_0 points in the $+\hat{\mathbf{z}}_{\text{hybrid}}$ direction and $\hat{\mathbf{Y}}$ points in the $\hat{\mathbf{Y}}_{\text{hybrid}}$ direction. Since Ω_0 is exact, the surface in this hybrid frame is known exactly. The hybrid frame differs from the body-fixed frame only by a rotation around $\hat{\mathbf{z}}_{\text{hybrid}}$ of γ_0 . Such rotations affect density moments via

$$K_{\ell m}^{\text{hybrid}} = e^{-im\gamma_0} K_{\ell m}^{\text{body-fixed}}. \quad (8)$$

by equation A9. Thus, uncertainty on $K_{\ell m}^{\text{body-fixed}}$ (obtained from the encounter data) can be translated to uncertainty in $K_{\ell m}^{\text{hybrid}}$. From now on, we will operate only in the hybrid frame and suppress the label.

To extract a density distribution for the asteroid, we divide the asteroid into N finite elements of uniform density. When the K_{3m} are extracted, 16 moments are known. However, one of these is redundant with the mass of the asteroid, which must be fixed since density cannot be determined absolutely. Six more are redundant with the position and orientation of the coordinate axes, such that only nine finite elements are free. On all the N densities, we place constraints that $0.25 < \rho < 3$, in units where the average density of the asteroid is one (i.e., the mass of the asteroid is set equal to the volume).

JTD: Continue description

3 RESULTS

To demonstrate our interior-probing methodology, we provide a full density distribution retrieval applied to synthetic data for the asymmetric reference asteroid. We first introduce the retrieval capabilities regarding density moments, then we turn to the constraints that can be derived reliably on the density distribution. For both level of information retrieval, we find that the results are consistent with the properties used to generate the synthetic data.

3.1 Density moments

Figure 2 shows our synthetic spin data. The best-fitting model is overlaid in the top panel and residuals are shown in the bottom panel. Uncertainties are plotted on the residuals corresponding to the square root of the diagonal entries of the covariance matrix (correlations not included). The fit results are clearly consistent with the data.

Figure 3 shows a corner plot of the PPDs of the ten parameters (namely γ_0 and $K_{\ell m}$ for $\ell \leq 3$), marginalized to functions of one (histograms) or two (contours) variables. The true parameters are shown as lines. Note that the true parameters usually lie within 1 or 2σ of the $\Delta K_{\ell m} = 0$, where $\Delta K_{\ell m}$ is the difference between the posterior $K_{\ell m}$ and the true $K_{\ell m}$. The PPDs are generally Gaussian and sometimes show correlation between parameters, but no continuous degeneracy occurs. We performed 48 independent minimizations of the likelihood before the MCMC fit began, each with an initial point chosen randomly in the parameter space. All converged to the same minimum, demonstrating that the model lacks discrete degeneracy as well.

3.2 Density distribution

Figure 4 shows the density distributions and uncertainties extracted for the asymmetric reference asteroid. These distributions were made given the density moment PPDs extracted above, with a_A fixed. The surface is fixed as a triaxial ellipsoid with semi-axis lengths such that the true values of $K_{\ell m}$ are consistent with uniform density (equation A4).

Also in each panel of figure 4 is χ_r^2 , or reduced chi squared value, defined as the average of the squared differences between the fitted density moments and the density moments of the final distribution divided by the fit uncertainties. This fit metric is non-zero due to numerical error in the likelihood model case, which is guaranteed to exactly reproduce $K_{\ell m}$. The harmonic and lumpy models have no such guarantee, however.

The likelihood and harmonic models produce nearly identical density distributions. This is generally true for uniform density asteroids, which have harmonic density distributions. Consequentially, χ_r^2 is relatively low for the harmonic model. This similarity lends confidence to both models, because if one were unexpectedly biased towards certain distributions, the other would have to be equally biased in the same way in this case to produce the same distribution, which appears unlikely given that the models share little in common.

The distributions are non-uniform for the harmonic and likelihood models (driven by error in the estimates of K_{3m}), but the non-uniformity is limited. The second row of figures indicates that 95% of the asteroid lies within 39% of the true density distribution for the likelihood and harmonic models. The lumpy model yields a much more uniform distribution because it is designed to produce uniform lumps. However, it produces a density distribution less consistent with the moments extracted from spin data than the previous two models (i.e., χ_r^2 is large). This is because the lump found extends outside the asteroid, violating the assumptions of the model, which is a sign that the lump found does not really exist inside the asteroid.

The third row of figures indicates that density distribu-

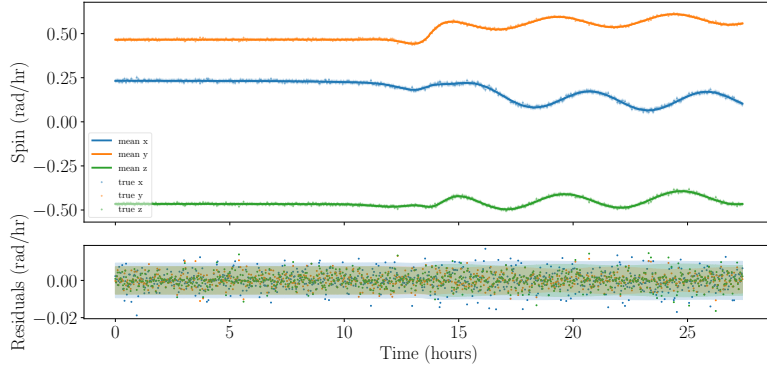


Figure 2. Data, best-fitting results, and residuals for a fit to synthetic data simulated for an asymmetric reference asteroid. Uncertainty bands are also shown. The best fit results appear consistent with the data.

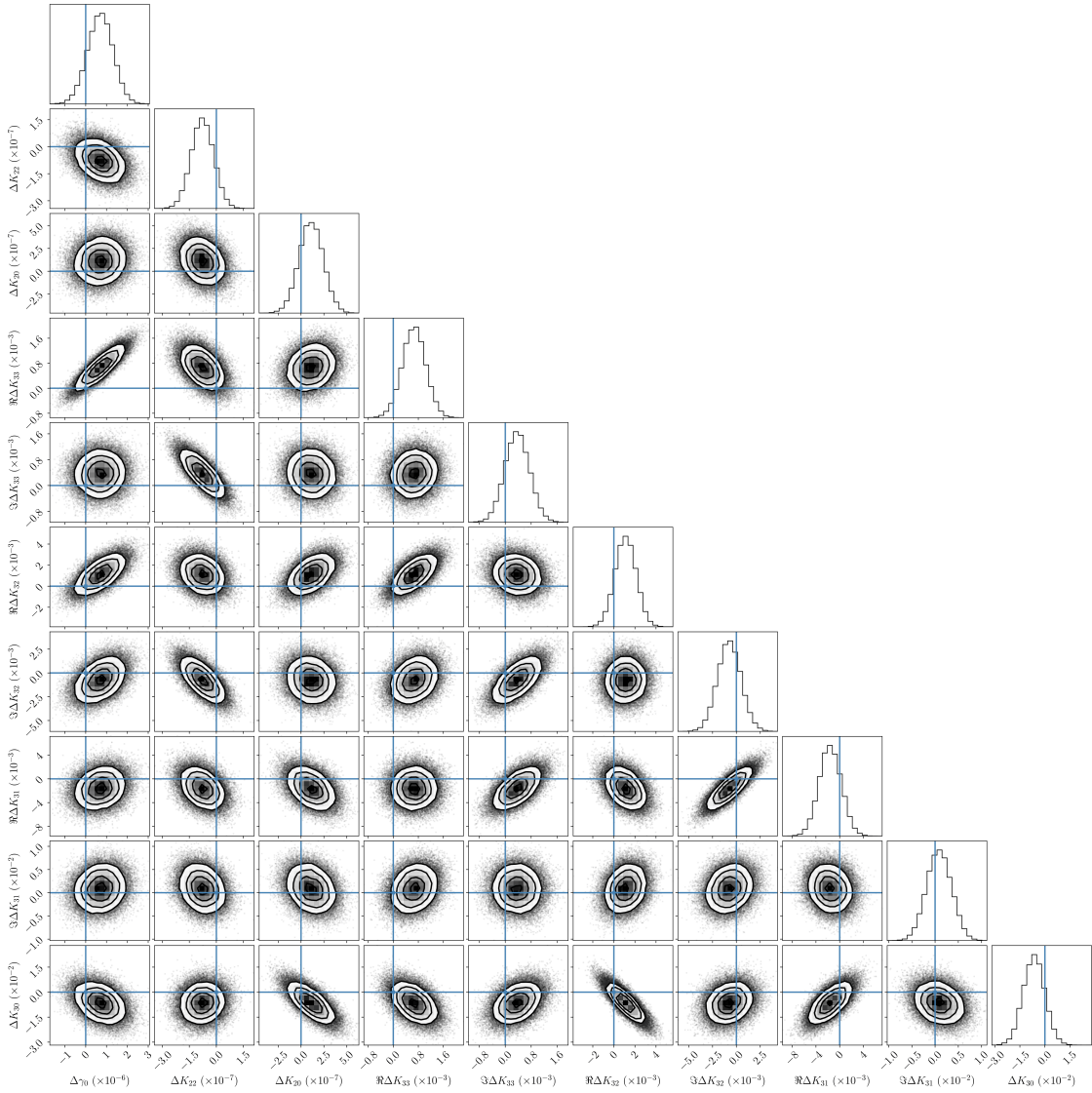


Figure 3. PPDs extracted from synthetic encounter data for the asymmetric reference asteroid. Samples from the MCMC fit are shown as individual points, and the contours enclose 1, 2, and 3 σ confidence regions. True values are shown as blue lines. PPDs are Gaussian and show no degeneracies.

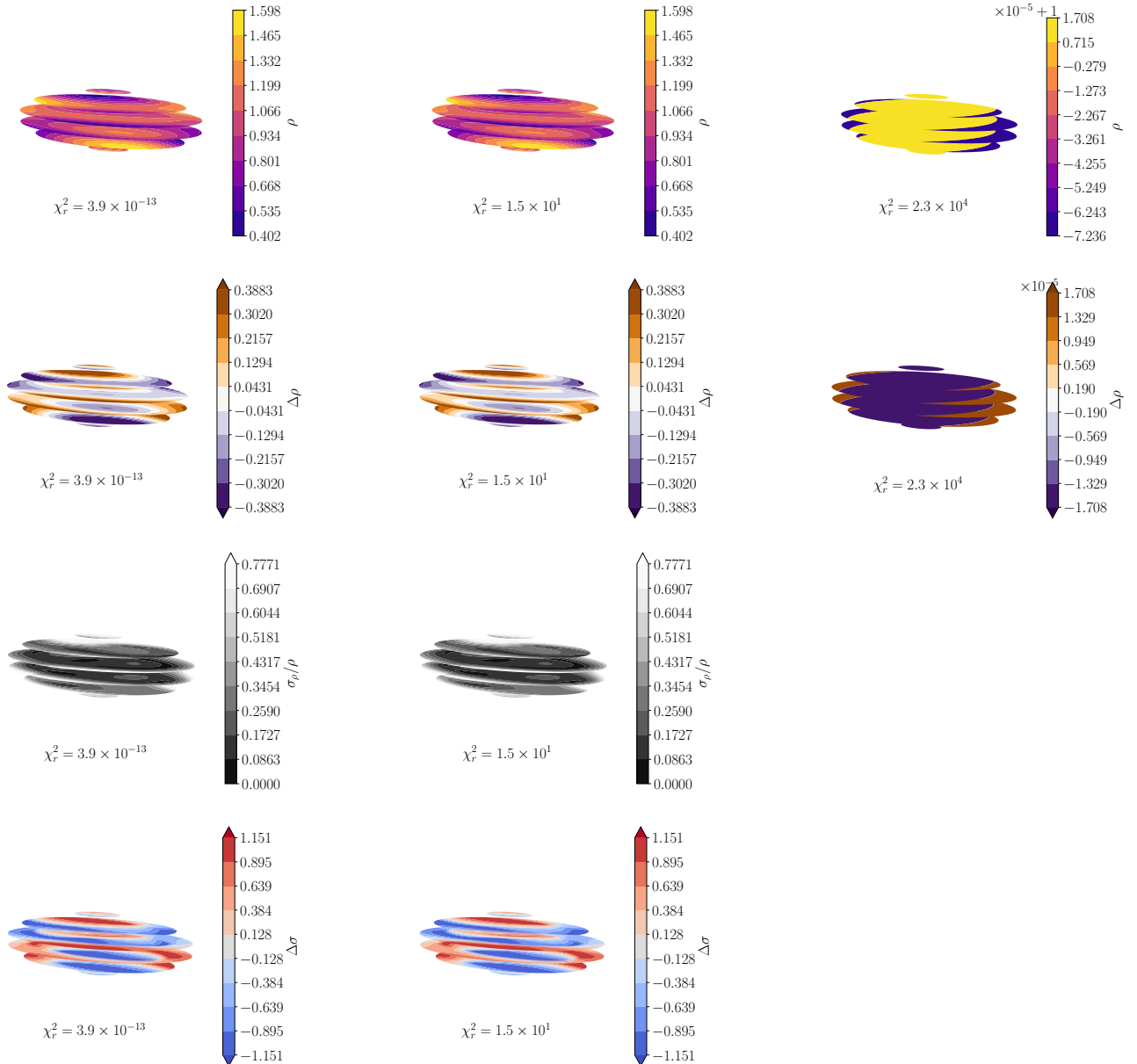


Figure 4. Based on density moments extracted from synthetic data of the uniform-density asymmetric reference asteroid encounter, the following are shown. From top to bottom, the density distributions extracted by the methods of section 2.4, their deviations from the true distributions, uncertainties, and the ratio of deviations to uncertainty. For the bottom three rows, color map range is chosen to include 95% of the asteroid to suppress outliers. The models used are likelihood (*left*), harmonic (*middle*), and lumpy with $d = N = 1$ (*right*). Density is normalized so that mean density is one. Density is consistent with uniform in all cases ($\lesssim 1\sigma$ deviation), and typically differs from uniform by little more than 40%.

tion uncertainty can extend to 78% of the local density, but most of the asteroid is well below this value. Uncertainty is generally larger towards the edges of the distribution, both for these shapes and for the shapes shown later. The fourth row indicates that for 95% of the asteroid, the density distribution is within 1σ of the true, uniform distribution. Uncertainty plots are not generated for the lumpy model because the distribution is not continuous; each point in the asteroid can only take one of two density values, depending on whether it is inside the asteroid or outside it.

To test the ability of our methodology to identify dis-

crete changes in density distribution of the kind that the lumpy model is designed to detect, we show another example extraction. We place a spherical mass of density six times that of the surrounding medium inside the asymmetric reference asteroid, slightly displaced along $\hat{\mathbf{y}}$. Both the mass and the medium have uniform density. The density moments are extracted and density distributions made via the three models and are shown in figure 5.

We see from figure 5 that the harmonic and likelihood model fail to recover the presence or location of the lump, in that the top row shows a smoothly varying distribution

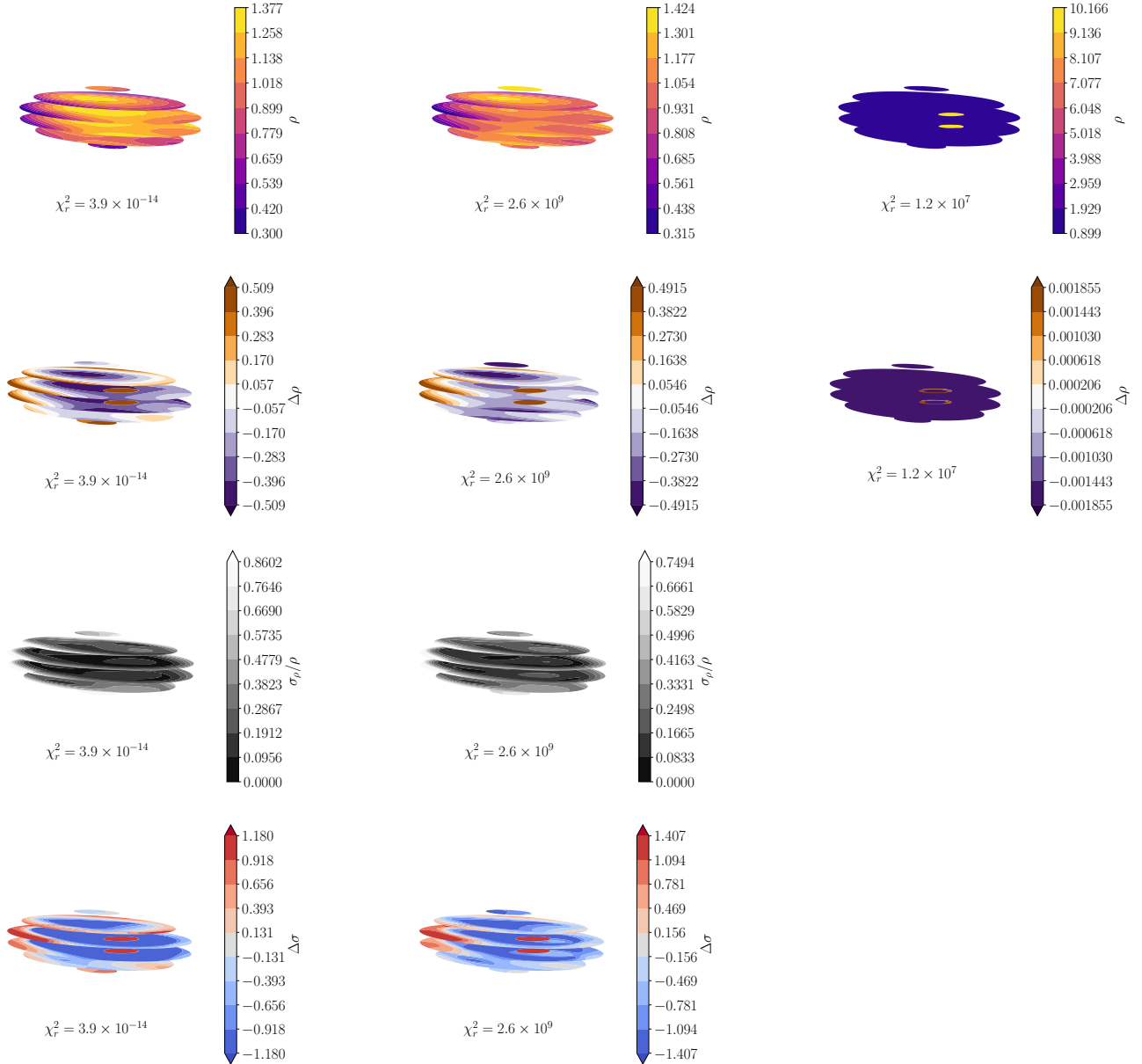


Figure 5. Density distributions and uncertainties for the asymmetric reference asteroid encounter with an off-center lump. See figure 4 for a description of each panel.

while the second row shows that the distribution is too low by a factor of half the mean density in the region of the lump. In the case of the likelihood model, the density is also twice the mean just outside the lump boundary, indicating that the model has identified the general location of the lump but cannot refine its radius and resolve the lump's edge. Unlike the previous example, the harmonic and likelihood models do not agree exactly, and χ^2_r is large for the harmonic model. These two facts arise from the fact that the true distribution is not harmonic.

The uncertainty plots (lower two rows) of figure 5 show consistency with the true distribution (within 1.2σ for 95% of the asteroid), although uncertainties are larger for this non-uniform case than they were for figure 4. The uncer-

tainty rises to as much as 85% of the local density as opposed to 78% in the former case.

The failure of the harmonic and likelihood models to find lumps is expected, since K_{2m} and K_{3m} are only sensitive to large-scale non-uniformities. However, the lumpy model computes the location and density of the mass very well. Some inaccuracies are induced by the uncertainty in K_{3m} , which changes the minimum of equation ?? such that the lump is displaced by 9 m along \hat{y} from where it should be. This in turn causes a 70 m difference between the extracted lump's radius and the true radius. There is therefore a 70 m-thick shell surrounding the lump produced by the lumpy model which has been inaccurately estimated, but this shell contains less than 5% of the asteroid. The scale of figure 5 shows that, for the rest of the asteroid, the density is

estimated accurately to about two parts in one thousand. This model produces a χ^2_r lower than the harmonic model, indicative of its accuracy.

It seems that the lumpy model is capable of recreating the location of lumps. But the ability of the lumpy model to place a lump does not guarantee the lump to exist, as was seen in figure 4.

JTD: Note for Julien: the cutoffs on the color bars (95% of the asteroid) are kind of arbitrary. I could make histograms showing, on the vertical axis, $\Delta\sigma$ or σ_ρ/ρ or $\Delta\rho$ (i.e., the metrics which are plotted in these figures). On the vertical axis, I would plot what fraction of the asteroid has these values. So you would expect to see that most of the asteroid has $\Delta\rho$ small, and then there's a cutoff beyond which only a small fraction of the asteroid has larger $\Delta\rho$. Do you think this plot is worth the space?

4 DISCUSSION

4.1 Dependence of parameter uncertainty on encounter properties

In this section, we discuss how the precision of the best-fitting density moments is affected by various encounter properties. We call this precision “posterior uncertainty,” or $\sigma(K_{\ell m})$, defining 1σ posterior uncertainty as the range containing 68.27% of the PPD centred on the median. 2σ posterior uncertainty is defined likewise for 95.45% of the PPD. These are roughly equivalent to 1 or 2 times standard deviation of the PPD respectively. We use the configuration of the asymmetric reference asteroid (appendix B) unless otherwise stated.

It will be useful to have a rule-of-thumb “posterior uncertainty threshold,” above which we say that posterior uncertainty $\sigma(K_{\ell m})$ is too large to yield meaningful estimates of density distribution. We define this posterior uncertainty threshold as the point at which the median of the ratio between the local density uncertainty and local density (ρ_σ/ρ) is equal to a fraction f . For this analysis, we investigate both $f = 100\%$ (corresponding to an essentially unconstrained density distribution) and $f = 20\%$.

We use this threshold because it has clear physical meaning, unlike the density moments. But the value of ρ_σ/ρ depends on the model used, unlike $\sigma(K_{\ell m})$. In this analysis, we use the likelihood model, but choosing a different model with constraints added would reduce density uncertainty, and lead to less restrictive thresholds.

4.1.1 Orbital elements

A Keplerian orbit is completely described by five parameters, but three describe the orbit’s orientation with respect to the central body. They are therefore redundant with the orientation of the inertial frame and we do not investigate them here. We parametrize the remaining two parameters by the perigee distance r_p and excess velocity v_∞ . Fits of the type described in section 2.3 were run for many values of r_p and v_∞ and the 1 and 2σ posterior uncertainties are displayed in figure 6.

Encounter property	$\sigma_\rho/\rho = 100\%$	20%
Perigee (r_p , Earth radii)	<7.9	<4.7
Spin pole uncertainty (σ_θ , $^\circ$)	<2.8	<0.5
Spin period uncertainty ($P_\omega \sigma_\rho$, ms)	<15	<3.1
Asteroid length (a_A , m)	>180	>1100
Cadence (Δt , min)	<38	<2
Data gap (T_{gap} , hr)	<1.8	<0
Period (P_ω , hr)	>4.3	>9.5

Table 1. For each encounter property discussed in section 4, the properties that lead to density uncertainty equal to 100% (20%) of the local density are shown in the middle (right) columns. The reference asymmetric asteroid is used. The 20% threshold is very restrictive, but the 100% threshold is more achievable and demonstrates the thresholds in the right column are not hard cut-offs.

Figure 6 demonstrates that posterior uncertainty follows a slight trend for uncertainty to increase with v_∞ . This is likely due to the fact that larger v_∞ leads to a faster and flatter orbit with less time spent close to the planet, where tidal torque is strongest. There are also comparatively large oscillations in the uncertainty, due to the orientation of the asteroid at perigee varying. (The asteroid is always simulated to start at the same orientation, but increasing v_∞ decreases the time to perigee so that the asteroid enters this region of high torque at different orientations depending on v_∞ .) Hence, the oscillations have the same period for all parameters. The dependence of posterior uncertainty on v_∞ is weak enough so that σ_ρ/ρ never reaches 100% for the v_∞ investigated.

The figure shows much stronger dependence of parameter uncertainty on perigee distance, as expected by the factor of $(a_A/D)^{\ell'}$ present in equation 3 and mentioned in section A3. For $r_p = 7.9$ Earth radii, σ_ρ/ρ reaches the 100% threshold. The 20% threshold is reached at lower 4.7 Earth radii. Much of this uncertainty is dominated by uncertainty in K_{30} , which is the parameter least constrained by tidal torque analysis. At $r_p \approx 10$ Earth radii, K_{30} fills the prior distribution with uncertainty ranging from -1 to 1, visible by the sudden cut-off in uncertainty increase and the discontinuity of the $\sigma(K_{\ell m})$ curve there.

The axes of figure 6 show that parameters with large m are more precisely determined than parameters with small m , as can be seen by comparing K_{22} to K_{20} and comparing K_{33} to other K_{3m} values. Large m moments correspond to moments that control higher frequency fluctuations in density at the asteroid equator. This pattern of $\sigma(K_{\ell m})$ smaller for large m is a general trend and will be seen in the following sections as well.

The very strong dependence of $\sigma(K_{\ell m})$ on r_p makes this analysis most useful to extract second-order moments on close encounters. Fortunately, in the case of Earth, these encounters are also likely to have the best associated observational uncertainty when above the horizon due to their proximity. The first-order moments can still be extracted at much larger perigee distances in our model.

4.1.2 Observational uncertainty

Two parameters, σ_θ and σ_ρ , govern the observational uncertainty of the data set. These parameters are defined in section 2.2; σ_θ represents the standard deviation of the angle

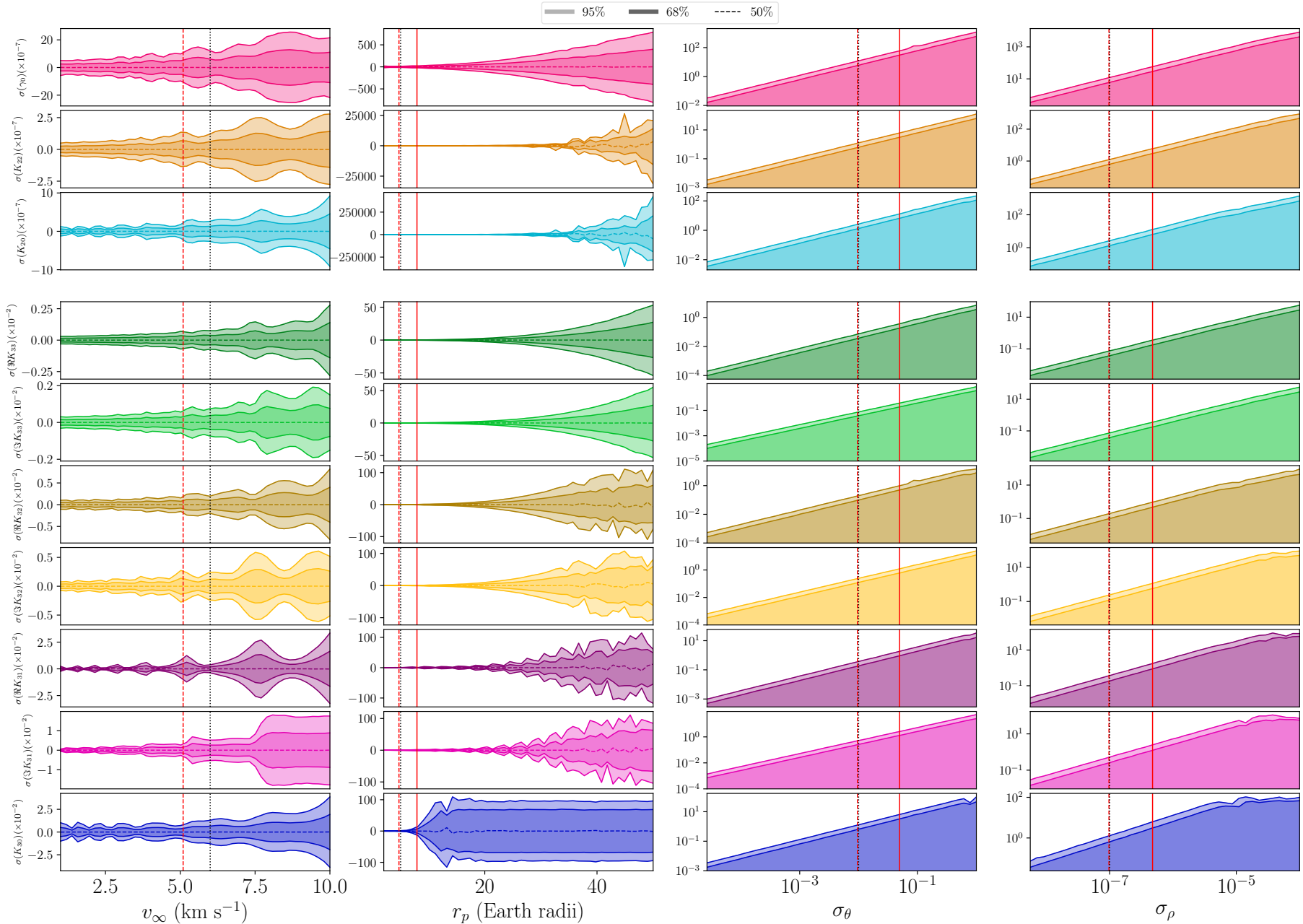


Figure 6. 1 and 2σ confidence intervals for the first-order parameter PPDs (*top*) and second-order parameters (*bottom*) as a function of (left to right) perigee, excess velocity, spin pole uncertainty, and period uncertainty. The vertical dashed line indicates the reference asteroid values. The red vertical lines indicate when $\sigma(K_{3m}) = 0.01$.

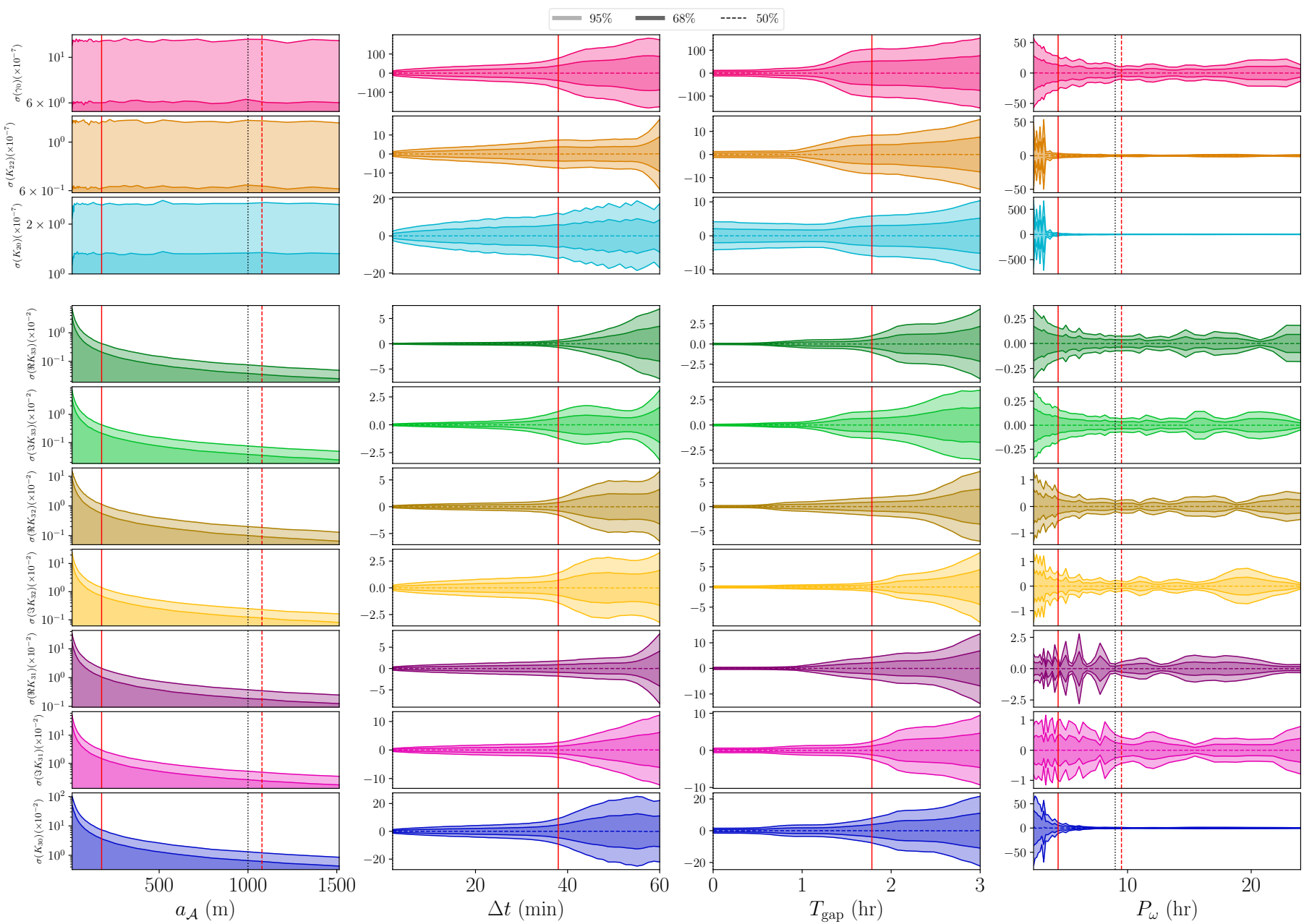


Figure 7. 1 and 2σ confidence intervals for the first-order parameter PPDs (*top*) and second-order parameters (*bottom*) as a function of (left to right) asteroid length, observational cadence, data gap at perigee, and rotational period. The vertical dashed line indicates the reference asteroid values. The red vertical lines indicate when $\sigma(K_{3m}) = 0.01$.

between the true spin pole and the observed spin pole, while σ_ρ represents the standard deviation of the ratio between the observed and true rotational velocities. Rather than explore the full space spanned by these two values, we fix one and allow the other to vary to better assess whether uncertainty in spin pole or uncertainty in period more strongly affects posterior uncertainty $\sigma(K_{\ell m})$. This dependence is displayed in figure 6.

For the case in which σ_ρ is held fixed and σ_θ is varied, the figure shows that the dependence of $\sigma(K_{\ell m})$ on σ_θ is linear. The uncertainty threshold is reached at $\sigma_\theta = 2.8^\circ$ (0.5°) for $\sigma_\rho/\rho = 100\%$ (20%). The K_{2m} uncertainties remain low, even for $\sigma_\theta \approx 1$, which is large enough that the spin pole has non-negligible probability to be observed in any direction.

If σ_ρ is allowed to vary instead, then K_{30} reaches the 100% and 20% thresholds at σ_ρ which correspond to period uncertainty of several milliseconds. At large period uncertainty, the PPDs begin to fill the prior and the posterior uncertainty $\sigma(K_{\ell m})$ is no longer linear with σ_ρ (this is especially visible in the K_{30} case). Otherwise, posterior uncertainty is proportional to σ_ρ .

These data show that posterior uncertainty is extremely sensitive to observational uncertainty in period in our analysis. To precisely measure density moments, very accurate rotational period estimates would have to be made for every angular velocity data point. However this analysis does not study the effect of collecting more data after the encounter, or the correlations between different angular velocity measurements. If these correlations were taken into account, or a more accurate uncertainty model used which took into account the asteroid's location in the sky or its distance to Earth, then the precision limit we find here will be affected.

4.1.3 Asteroid shape

The true values of $K_{\ell m}$ and a_A , which quantify the asteroid's physical properties, affect the posterior uncertainties. Here, we only investigate the sensitivity of $\sigma(K_{\ell m})$ to the first-order parameters and a_A . These K_{2m} moments can also be viewed as the axes of a uniform density triaxial ellipsoid (equation A4).

In figure 8, we show the 1σ posterior uncertainties as a function of K_{20} and K_{22} , or alternatively a/c and b/c . We use axis ratios rather than the values of a , b , and c because axis ratios are independent of a_A . The large $|K_{22}|$ sides of the K_{2m} -space plots correspond to asymmetric ellipsoids, as do the points far from the $a/c = b/c$ diagonal of the axis-ratio-space plots. The point corresponding to a sphere, which experiences no tidal torque and no tumbling, is at $K_{2m} = 0$ and $a/c = b/c = 1$.

The figure shows large uncertainty in γ_0 for $K_{22} = 0$, or $a/c = b/c$, because K_{20} is rotationally symmetric around \hat{z} , and γ_0 is the initial orientation with respect to the \hat{z} axis. The system then has no dependence on γ_0 when $K_{22} = 0$. This induces degeneracy in the model which inflates uncertainties, not only in γ_0 but also the other components.

To remove the inflated uncertainty, one could assume a rotationally symmetric asteroid, remove γ_0 as a parameter, and run a fit. For a nearly rotationally symmetric asteroid however, a new parametrization is necessary which does not contain the ill-constrained γ_0 parameter. This task is beyond

the scope of this paper, so we mostly consider asymmetric asteroids throughout.

Figure 8 also shows low uncertainty for highly asymmetric asteroids, where b/c and a/c are very different (i.e., when $|K_{22}|$ is large). Additionally, $\sigma(K_{20})$ and $\sigma(K_{22})$ decrease for large $|K_{20}|$, which corresponds to large axis ratios in the ellipsoid case.

Figure 9 displays the correlation between the first-order parameters. They show that γ_0 and K_{22} are often correlated for asymmetric asteroids, while γ_0 and K_{20} are usually not. This is expected as K_{22} is dependent on the orientation of the asteroid and K_{20} is not. They also show that K_{22} and K_{20} are usually correlated, and that a/c and b/c are highly correlated. The latter is expected due to the $1/c$ dependence.

The fact that $K_{\ell m}$ are correlated indicates that, in order to correctly propagate density moment uncertainties to a density distribution, a full PPD is necessary. If only 1σ uncertainty intervals for each parameter were used, density distribution uncertainty would be overestimated. This full PPD is produced by our fit process, but only the 1σ uncertainties are displayed in this paper in most cases.

Overall, the variation in the uncertainties on K_{20} and K_{22} (the first-order density moments) is present but largely smooth across their allowed parameter space, as is their correlation. It therefore seems reasonable to use the asymmetric asteroid shape as a stand-in for an unknown's asteroid shape when simulating an encounter, as we do in this paper. The uncertainty then can be expected to differ across other shapes by a factor of about two or less, as long as the degenerate, symmetric asteroid regime is avoided.

On the other hand, the posterior uncertainty of K_{3m} is much more strongly dependent on asteroid length a_A . Figure 7 displays posterior uncertainty $\sigma(K_{\ell m})$ as a function of a_A . As was mentioned in section A3, the K_{2m} parameters are insensitive to a_A since the a_A^2 term in τ (equation 3) cancels the a_A^2 in the moment of inertia (equation 4). The K_{3m} uncertainty is strongly dependent on a_A for the same reason that it is dependent on r_p : the $(a_A/D)^{\ell'}$ dependence of equation 3. At $a_A \leq 1100$ m, $\sigma_\rho/\rho \approx 100\%$. However, the 20% cut-off is much lower, at $a_A \leq 180$. Figure 7 demonstrates why these cut-offs are so distant; for large a_A , uncertainty decreases slowly with length. Only for small lengths is the uncertainty very large. This behaviour indicates that the uncertainty threshold is unlikely to fall much below 180 m even if other properties of the encounter are adjusted.

For uniform density asteroids, large a_A is equivalent to large asteroid radius. In non-uniform density asteroids, large a_A can also be achieved by distributing the mass of the asteroid near the surface, because the r^2 term in the integrand of the definition of a_A causes the density of regions distant from the asteroid centre of mass to dominate a_A .

4.1.4 Cadence

The time between observations of asteroid angular velocity, or cadence, may vary depending on the observational schedule of the observing telescopes and the path of the asteroid through the sky. We measure how the posterior uncertainty $\sigma(K_{\ell m})$ varies with cadence ranging from two minutes to one hour in figure 7.

Figure 7 displays little dependence of uncertainty on cadence Δt for $\Delta t \lesssim 40$ min. We also see flaring of uncer-

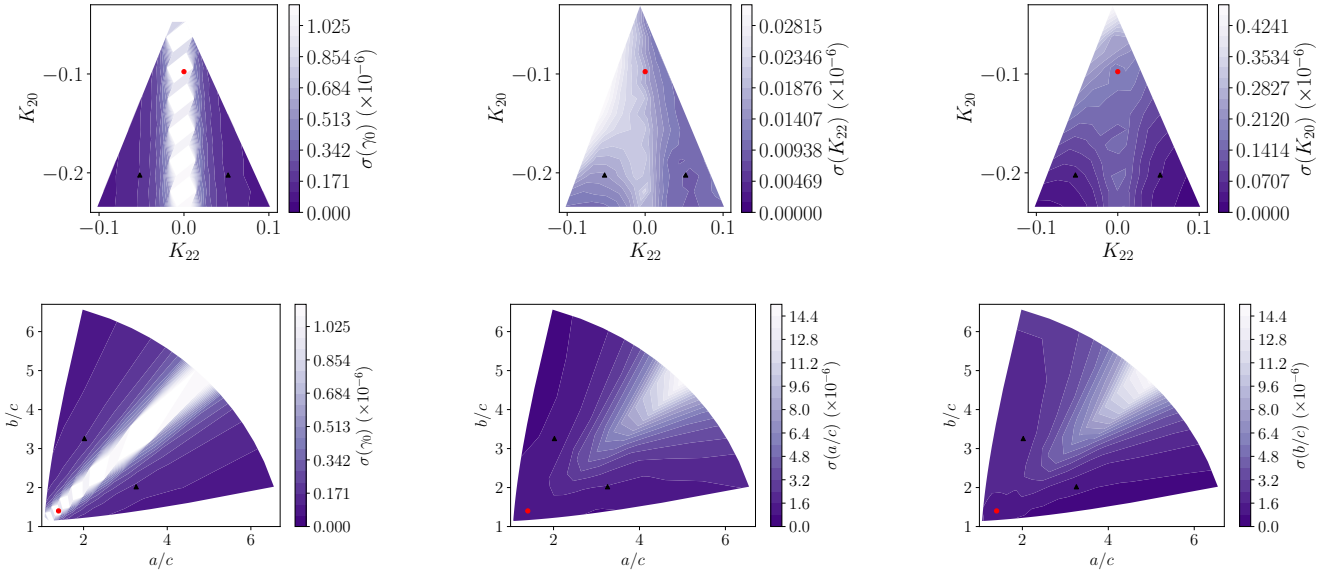


Figure 8. 1σ posterior uncertainty for first-order parameters γ_0 , K_{22} , and K_{20} (top row) and γ_0 , a/c , and b/c (bottom row). Also shown as black points are the reference asteroid shapes: symmetric (red circle) and asymmetric (black triangle). Symmetric asteroids ($K_{22} = 0$ or $a/c = b/c$) show increased posterior uncertainty, but otherwise posterior uncertainty is roughly constant.

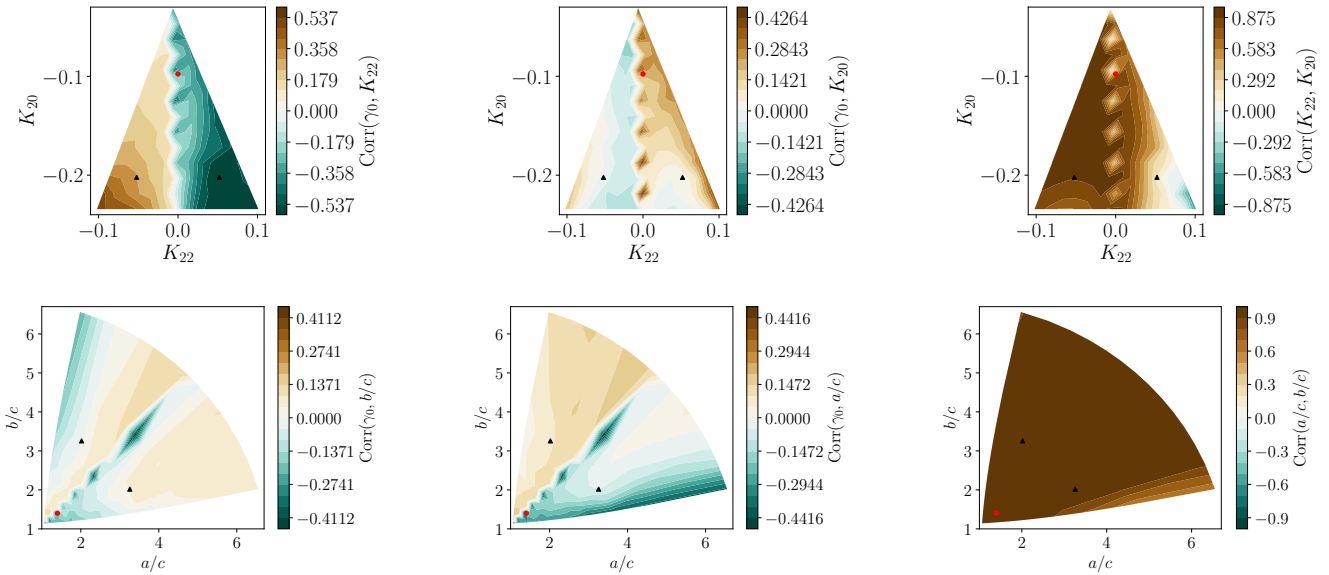


Figure 9. Correlations between PPDs for first-order parameters γ_0 , K_{22} , and K_{20} (top row) and γ_0 , a/c , and b/c (bottom row). Also shown as black points are the reference asteroid shapes: symmetric (red circle) and asymmetric (black triangle). The first order parameters K_{22} and K_{20} are correlated, as are initial orientation γ_0 and K_{22} .

tainty for very large cadence, largely driven by the paucity of data points. However, uncertainty dramatically increases for many parameters at about $\Delta t = 30 - 40$ min, a time scale which is likely characteristic of the asteroid system. We name this rough cadence limit T_{cad} . T_{cad} is also the location at which the $\sigma(K_{3m})$ threshold is crossed for all second-order moments except K_{30} , which exceeds the uncertainty threshold at $\Delta t \approx 5$ min.

We expect this T_{cad} to be a function of two dynamical time scales of the system: the rotational period of the

asteroid P_ω and the dynamical time scale of the orbit (the latter can be estimated in multiple ways, since both r_p/v_∞ and $v_\infty r_p^2/\mu_B$ have units of time and may be relevant). How these time scales affect T_{cad} is discussed in appendix D.

Figure 7 shows that as long as $\Delta t < T_{\text{cad}}$ is achieved, the influence of cadence on σ is minimal, but shorter cadence leads to lower uncertainties.

4.1.5 Perigee gap

In certain circumstances, spin data might not be able to be captured for a close encounter at perigee. The asteroid might dip below the horizon, or it might pass too close to the sun to be observed. Generally, angular velocity data can be collected when the asteroid is distant from the central body, where torque is low. There, the angular velocity evolution is dominated by torque-free precession dictated by the moment of inertia components. That zero-torque data can still be used to fix K_{20} and K_{22} as in Moskovitz et al. (2020). However, K_{3m} does not affect the precession periods (though they do affect the phase). We are therefore curious as to how our posterior uncertainties change due to lack of perigee data.

To test this, we mask the perigee of the counter by removing a duration T_{gap} of data centred on the perigee, where T_{gap} ranges from 0 to 3 hours. To prevent lack of precision on $K_{\ell m}$ induced by lower amounts of data for high T_{gap} , we always cut 3 hr – T_{gap} from the data set, half from the beginning and half from the end, so that each data set produced for all T_{gap} has the same size. We then fit the same asteroid model to the cut data for all T_{gap} and plot posterior uncertainties $\sigma(K_{\ell m})$ in figure 7.

Since torque is greatest at perigee, we expect that region of the data to contain the most information about $K_{\ell m}$, and therefore uncertainty should increase monotonically with T_{gap} , which is seen in figure 7. We also see that the first-order parameters are not as sensitive to T_{gap} as the second-order parameters, because K_{2m} are additionally constrained by torque-free precession after perigee.

Most parameters show dramatically increased uncertainty in the $T \sim 1 - 2$ hr range. On the other hand, none of the uncertainties increase noticeably for $T \lesssim 1$ hr. Thirty minutes of dropped data is equivalent to fifteen dropped points for the simulated cadence of $\Delta t = 2$ minutes, showing that many data points can be dropped from the data set at perigee before the uncertainty starts to increase.

Qualitatively, 7 shows similar dependence of $\sigma(K_{\ell m})$ on T_{gap} as on cadence Δt ; they also both have cut-offs where uncertainty markedly increases, and both the T_{gap} and Δt cut-offs have qualitatively similar shapes although they occur at different values of Δt and T_{gap} . This suggests that the factors that govern uncertainty due to cadence also may govern sensitivity to lack of data at perigee in a similar way.

4.1.6 Initial spin pole

The tidal torque experienced by the asteroid is affected by the initial direction of asteroid spin Ω_0 both because spin sets the initial asteroid orientation up to γ_0 and because of the spin-dependence of the rotational equations of motion (equation A14).

In figure 10, we display 1σ posterior uncertainties as a function of the direction of Ω_0 mapped onto the unit sphere in the inertial frame. Our samples for Ω_0 were laid out on a Fibonacci sphere to ensure they were roughly evenly spaced (marked in figure 11). To highlight common features across the parameters, we also display the average 1σ sensitivity in figure 11. The average is weighted such that the uncertainty map for each parameter contributes an equal amount (the weight of each map is set to one-tenth of the map's mean).

This average map is presented in two different projections to allow data at $\hat{\mathbf{Z}}$ to be read.

Certain alignments of the body-fixed frame to the inertial frame lead to special conditions on torque, as discussed in section A3. For example, $\mathbf{z} \parallel \hat{\mathbf{Z}}$ and $\mathbf{z} \parallel \hat{\mathbf{Y}}$ at perigee lead to $\boldsymbol{\tau} \parallel \hat{\mathbf{z}}$ to first-order, and $\boldsymbol{\tau} \parallel \hat{\mathbf{X}}$ at perigee leads to $\boldsymbol{\tau} = 0$ to first-order. We relate this to the initial direction of Ω_0 , via the approximation that $\boldsymbol{\tau}$ is small until perigee. Then $\Omega_0 \parallel \hat{\mathbf{Y}}$ and $\Omega_0 \parallel \hat{\mathbf{Z}}$ both lead to $\boldsymbol{\tau} \parallel \hat{\mathbf{z}}$, and $\Omega_0 \parallel \hat{\mathbf{X}}$ leads to $\boldsymbol{\tau} = 0$.

Figure 11 shows area of increased uncertainty for $\Omega_0 \parallel \hat{\mathbf{Z}}$ and $\Omega_0 \parallel \hat{\mathbf{Y}}$, but not the $\hat{\mathbf{X}}$ case. This indicates that $\boldsymbol{\tau} \parallel \hat{\mathbf{z}}$ causes increased uncertainty. Physically, $\boldsymbol{\tau} \parallel \hat{\mathbf{z}}$ only changes an asteroid's rotational period and does not cause it to tumble, eliminating the ability to discern moment of inertia ratios from zero-torque precession after the encounter. If $\boldsymbol{\tau} = 0$ to first-order, then second-order $\boldsymbol{\tau}$ and non-perigee $\boldsymbol{\tau}$ will dominate, which may increase precision to these usually non-dominant parameters and therefore not have the same increasing effect on $\sigma(K_{\ell m})$.

However, uncertainty does not vary by much more than a factor of two outside the imprecise regions of $\Omega_0 \parallel \hat{\mathbf{Z}}$ and $\Omega_0 \parallel \hat{\mathbf{Y}}$, though these regions are wide for some parameters. Within the imprecise regions, uncertainty can grow up to four times or more the uncertainty at other Ω_0 values, and can exceed the $\sigma(K_{3m}) \approx 0.01$ threshold. The trends for are roughly consistent across parameters (figure 10), leading to clearly visible imprecise regions in the average $\sigma(K_{\ell m})$ (figure 11).

4.1.7 Rotational period

We also study the effect of the initial rotational period of the asteroid P_ω on posterior uncertainty $\sigma(K_{\ell m})$. In figure 7, we show $\sigma(K_{\ell m})$ as a function of P_ω for a range of periods typical of NEOs. Like figure 6, depicting the dependence of $\sigma(K_{\ell m})$ on v_∞ , figure 7 shows small-scale variation in uncertainty due to the fact that varying the initial period changes the value of γ at perigee, which affects uncertainty to a factor of about two. But a large-scale trend is also visible in many parameters. K_{20} and K_{22} show very large uncertainty for $P_\omega \lesssim 4$ hr because these fast-rotators tumble very little after perigee. This increases uncertainty on the K_{2m} parameters, which are constrained by tumbling.

We expect that quickly rotating asteroids would not tumble because, for small P_ω , the dynamical variables \mathbf{D} , $\boldsymbol{\omega}$, α , and β vary much smaller than γ . Approximating each variable as constant over one full rotation of γ , we can integrate the first-order contribution of $\boldsymbol{\tau}$ over $\gamma \in (0, 2\pi)$, which gives no secular, first-order torque to force the asteroid to tumble. However, this effect does not apply to the second-order parameters, since the integral over the second-order term of $\boldsymbol{\tau}$ does not vanish, as seen in the figure.

Another feature of figure 7 is that $K_{\ell 0}$ is more uncertain at low P_ω than the other parameters. This is most visible in the figure for K_{30} . The cause is likely that $K_{\ell 0}$ cannot contribute to τ_z as shown in equation 3. We already discussed that asteroids with small P_ω do not tumble, and since τ_x and τ_y are what induces tumbling, the most observable component of torque is therefore τ_z , which $K_{\ell 0}$ do not affect.

The most severe effect of period on $\sigma(K_{\ell m})$ is in the low-period regime ($P_\omega < 4.3$ hr), but in this case, the most

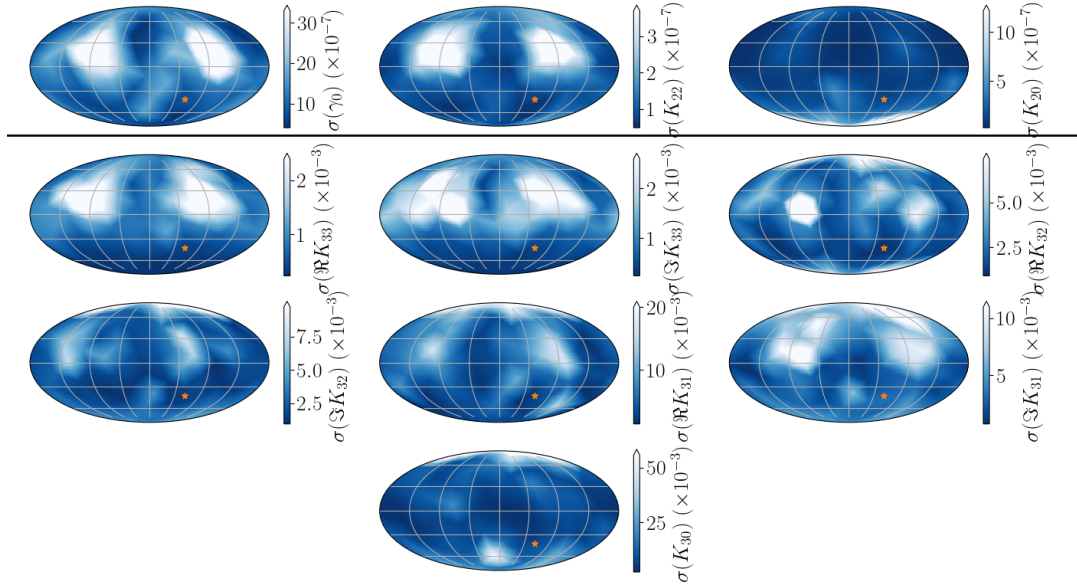


Figure 10. 1σ uncertainties for the first-order parameters (top) and second-order (bottom) as a function of the initial direction of spin in the inertial frame. All maps are made in the Mollweide projection. The orange star indicates the reference spin pole. The red contours enclose regions the 20% (dotted) and 100% (solid) σ_ρ/ρ cut-off. Posterior uncertainty depends similarly on initial spin pole direction for all parameters

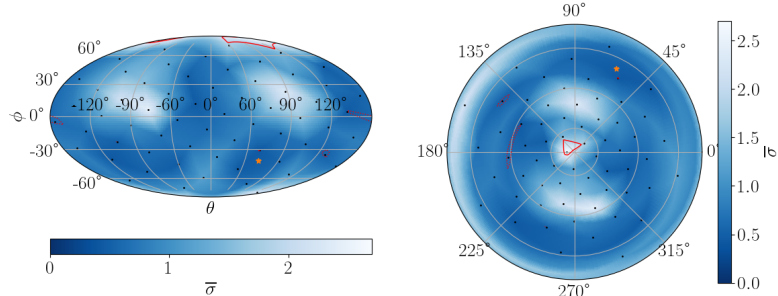


Figure 11. The weighted average of the uncertainties shown in figure 10, in Mollweide (left) and polar (right) projections in the inertial frame. See text for a description of how the average was computed. Black dots indicate the Fibonacci-sphere-distributed locations of sample spin poles, and the orange star indicates the reference spin pole. The polar projection is centred at the north pole, or $\hat{\mathbf{Z}}$. Posterior uncertainty is large near $\pm\hat{\mathbf{Z}}$ and $\pm\hat{\mathbf{Y}}$, but roughly constant elsewhere.

strongly affected parameters are K_{2m} , which are generally known better than K_{3m} . The effect on the imprecise parameters K_{3m} is small, except for K_{30} . It therefore seems as though small-period asteroids are still candidates for observation, although high-period asteroids yield smaller uncertainty.

4.1.8 Central body oblateness

In all the above studies, we assumed a spherical planet ($J_{\ell m} = 0$ for $\ell \geq 1$). By assumption that $\mu_B \gg \mu_A$ (so that the asteroid orbit's focus is the centre of mass of the central body), we have $J_{1m} = 0$. The effect of central body non-sphericity, then, is limited to the J_{2m} terms and damped by a factor of $(a_B/D)^2$. We expect these parameters to have small effect on the asteroid.

Here, we define oblateness as $\epsilon = (I_z - I_x)/(\mu_B R_B^2)$,

where $I_{x,y,z}$ are the central body moments of inertia along the principal axes, and $I_x = I_y$. R_B is the true radius of the body (not a_B from equation A3).

$J_{\ell m}$ is defined in equation A3 with respect to the asteroid orbit, not the principal axes of the central body. However, for an equatorial orbit, the central body principal axes coincide with the asteroid orbit frame and we may express ϵ simply in terms of $J_{\ell m}$ as $\epsilon = -10J_{20}/3$ and $J_{22} = 0$. For simplicity, we use this equatorial orbit case. Since an oblate ellipsoid is mirror-symmetric around all three axes, table A1 indicates that J_{3m} are all zero. The next order of tidal torque is therefore J_{4m} , damped by an additional $(a_B/D)^2$ factor, and non-ellipsoid corrections to the central body shape. We do not consider these extra factors.

Given this conversion between ϵ and J_{20} , we analyze posterior uncertainty $\sigma(K_{2m})$ of the first-order parameters as a function of ϵ across a reasonable range of central body

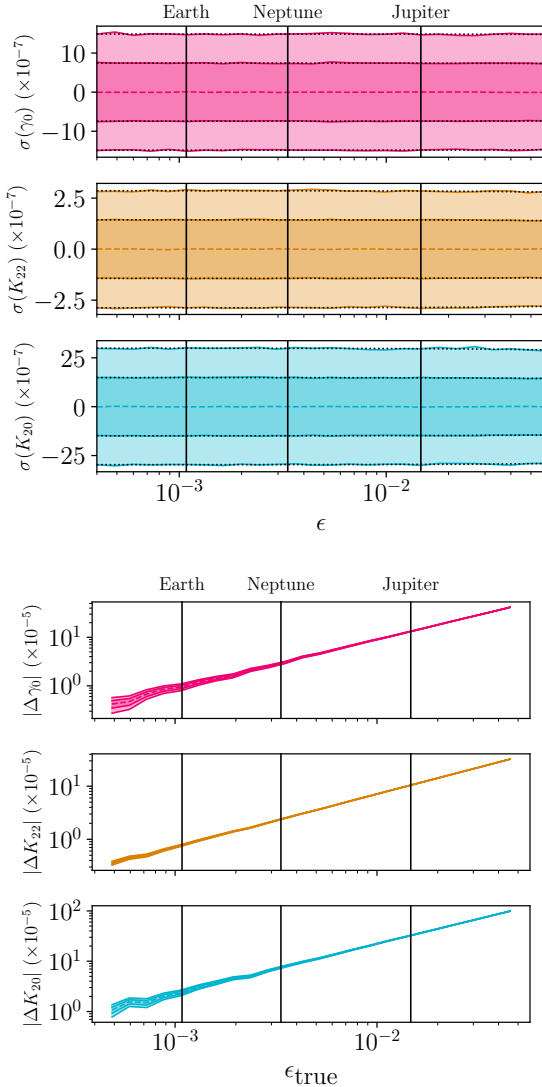


Figure 12. Top: 1 and 2 σ confidence intervals for the first-order parameter PPDs as a function of oblateness ϵ . Linear best-fitting lines to $\sigma(K_{2m})$ (black, dotted) are plotted. Bottom: The difference between PPD means extracted from a zero-oblateness model and the true parameters given data with true oblateness $\epsilon_{\text{true}} \neq 0$. Also shown in both figures are the oblatenesses of reference Solar System bodies. Posterior uncertainty depends little on oblateness, but the best-fitting parameter estimates are affected enough by oblateness that oblateness must still be modelled.

oblatenesses based on those of Solar System planets Pater & Lissauer (2015). These uncertainties are shown in the top panel of figure 12, together with linear best-fitting curves. The figure demonstrates almost no dependence of $\sigma(K_{\ell m})$ on oblateness ϵ , although posterior uncertainty does measurably decrease for oblate central bodies. The best-fitting lines match the uncertainties well, and they have slope of $[\Delta\sigma(K_{\ell m})/\sigma(K_{\ell m})]_{\epsilon=0}/\Delta\epsilon = -0.06$ for γ_0 , -0.2 for K_{22} , and -0.3 for K_{20} . The second-order parameters K_{3m} likely depend on oblateness similarly, but fitting these parameters is computationally more expensive and we do not study them.

Note that if an encounter is executed around one of

the non-Earth objects noted in figure 12, a_B and μ_B will change in addition to ϵ . These two parameters also affect the posterior uncertainty (section 4.2), so the figure does not show that encounters with other bodies have the same precision as encounters with Earth; only that the difference in oblateness between the two bodies is of little concern.

Given the small effect of ϵ on $K_{\ell m}$, it might be tempting to neglect the planetary oblateness when fitting $K_{\ell m}$ to data. However, the bottom panel of figure 12 demonstrates that doing so is invalid. This figure displays $K_{\ell m}$ as extracted by a fit assuming $\epsilon = 0$, but run on data generated with non-zero ϵ . The difference between the PPD means and true parameters are shown. Posterior uncertainties are also shown as bands. The figure shows that even for low (Earth-scale) oblateness, the fit results are inconsistent with the true $K_{\ell m}$ values, since $\Delta K_{\ell m} = 0$ is not contained in the 2 σ band. This effect is much worse for large oblateness, growing to a difference on the order of $\mathcal{O}(100)\sigma$ for Jupiter's oblateness. Therefore, accurately modelling central-body oblateness to high precision is essential for accurate estimation of fit parameters. For non-equatorial orbits, with $J_{22} \neq 0$, we also expect J_{22} to affect the accuracy of the fit results to a similar degree, with the additional requirement of using the correct asteroid orbital plane.

J_{20} , the parameter studied in this section, has a slightly more general definition than oblateness. If the planet has a moon, the integral defining J_{20} (equation A3) can be extended to include this extra mass, though this can only be done when the asteroid never passes inside the moon's orbit. As an order-of-magnitude estimate for this effect, two spherical objects with masses and radii of Earth and the Moon, separated by one Lunar distance, and both lying in the orbital plane has a combined oblateness of $\epsilon = 0.82$. Extrapolating posterior uncertainties via the slopes of the best fit lines given earlier yields a reduction in $\sigma(K_{2m})$ by about 25%. Furthermore, J_{22} is non-zero for this case, which likely decreases posterior uncertainty even more.

This analysis suggests that large moons such as ours can improve fit quality, but further study of this effect is beyond the scope of this paper. Without a moon to inflate the oblateness of the central body, planetary oblateness does not significantly improve posterior uncertainty. However, correct representation of oblateness is essential to accurately estimate $K_{\ell m}$.

4.2 Comparison of Jupiter and Earth encounters

If sufficiently accurate spin pole data can be detected for non-Earth encounters, it may be possible to extract density moments for encounters with larger planets. In this section, we run our reference asteroid through a Jupiter encounter to analyze the differences in uncertainty.

The physical parameters of the asteroid body are kept the same as the Earth encounter case (listed in appendix B), as are the observational uncertainty and cadence. The orbit is adjusted for the Jupiter case by setting a perijove distance of $r_p = 5$ Jupiter radii (compared to perigee radius $r_p = 5$ Earth radii for the Earth encounter). The excess velocity does not strongly affect $\sigma(K_{\ell m})$ as shown in section 4.1.1, so we keep it at the reference value. The ratio between the posterior uncertainties in the Jupiter and the Earth encoun-

$K_{\ell m}$	$\sigma(K_{\ell m})_{\text{Jupiter}}/\sigma(K_{\ell m})_{\text{Earth}}$
γ_0	1.6
K_{22}	2.3
K_{20}	11
$\Re K_{33}$	18
$\Im K_{33}$	18
$\Re K_{32}$	18
$\Im K_{32}$	18
$\Re K_{31}$	25
$\Im K_{31}$	10
K_{30}	53

Table 2. Ratio of posterior uncertainty for all density moments $K_{\ell m}$ between an Earth encounter and a Jupiter encounter with identical properties except for an increased perigee. Observational uncertainty and cadence are assumed to be equivalent for the Jupiter and Earth encounters. Without taking the frequencies of close encounters into account, massive planets such as Jupiter yield less precise density moment estimates.

ters are shown in table 2. In all cases, the Jupiter posteriors are more uncertain than Earth posteriors.

These uncertainty ratios can be understood as follows. The leading order of tidal torque is proportional to μ_A/D^3 . If D/a_B (the ratio of the encounter distance to the central body radius) is roughly constant (as in this case, where $r_p/a_B = 5$), then $\mu_A/D^3 \propto \rho_B$ where ρ_B is the density of the central body. Therefore, little advantage is to be gained by looking for encounters of a massive planet in this sense. Since Jupiter is less dense than Earth, we expect that uncertainty in the first-order parameters γ_0 and K_{2m} would be slightly worse than in the case of Earth, which is seen in table 2.

The second-order terms are damped by an additional factor of a_A/D , which decreases if a massive central body is used. Since Jupiter is about 10 times larger in radius than Earth, we expect that the K_{3m} terms are about ten times more uncertain than the K_{2m} components, which is the case.

The $K_{\ell 0}$ components differ in that the posterior uncertainty increase for a Jupiter encounter over an Earth encounter is about five times greater for $K_{\ell 0}$ than other moments of the same ℓ . In fact, K_{30} essentially fills the prior. In section 4.1.6, we noted that $K_{\ell 0}$ is particularly uncertain when the asteroid does not tumble after the perigee. In this case, the Jupiter encounter resulted in less tumbling than the Earth encounter, so the larger increase in uncertainty in $K_{\ell 0}$ shown in table 2 is expected.

There are additional effects of central body mass which are not captured in this analysis. For example, encounters with massive planets are more plentiful, so that observation for a fixed period of time will lead to a larger number of observed encounters conducive to low-uncertainty moment extraction (large a_A , small r_p , etc.). The distribution of r_p in this encounter sample will also change; the ratio of the orbit impact parameter (the distance between the orbit asymptotes and the central body) to perijove distance is

$$\frac{b}{r_p} = \sqrt{1 + 2 \frac{G\mu_B}{r_p v_\infty^2}}. \quad (9)$$

It was mentioned above that the observable perigee distance r_p increases with $a_B \sim \mu_B^{1/3}$, so that $\frac{b}{r_p}$ is larger for more massive planets and therefore the same impact parameter leads to lower perijove. Other effects, such as a change in

the physical properties of the encountering asteroids or decreased observational uncertainty due to the distance between Jupiter and Earth-based telescopes, may also affect the fit uncertainties. Which of these contradicting effects dominates is not immediately clear, and depends on the asteroid population near Jupiter and the observation method.

4.3 Comparisons between density distribution models

To test the properties of the three density models defined in section 2.4 to extract density distributions from density moments, we simulate several asteroids with different shapes and density distributions on a close Earth encounter with the reference asteroid orbital and observational parameters. In all cases, the density moments are extracted via our fit process. Below, we compare the resulting distributions to understand the performance of the density distribution models.

4.3.1 Spherical asteroids

In this section, we test the sensitivity of the density distributions to incorrect estimates for the shape of the asteroid by assuming a spherical shape for the asymmetric and symmetric reference asteroids, with density distributions shown in figure 13.

Both the likelihood and harmonic models are accurate in that $\Delta K_{\ell m}^2$ is low, and they produce similar distributions as in the previous section. However, now even the asymmetric asteroid (with low uncertainty in $K_{\ell m}$) produces negative densities. This is a signal that the shape model is incorrect, and indeed the density distribution allows us to determine exactly how the shape model is wrong. In the asymmetric ellipsoid case, the density distribution is small (even negative) at large $|z|$ (top and bottom of the figure). The density is large at large $|y|$ (front right and back left in the figure). Comparison with the asymmetric reference asteroid depicted in figure 4 shows that the low-density region is outside the true asteroid shape, and the high-density region is inside. In other words, the shape can be corrected by extending it where density is large and retracting it where density is low.

A similar statement is true for the symmetric ellipsoid case in that density is low near the poles, but this time the regions with large density are evenly distributed around the equator, indicating the symmetry of the original asteroid.

The lumpy model produces lumps so large that they dominate the asteroid, predicting uniform distribution with $K_{\ell m} = 0$ for $\ell \geq 1$. The error in density moments $\Delta K_{\ell m}^2$ is therefore very large, equal to the sum of $|K_{\ell m}|^2$ for the original asteroids, making it clearly a poor model.

4.3.2 Nonuniform asteroids

We also test several non-uniform density asteroids and compare the generated density distributions for all three models to see if the non-uniformities are recovered. We consider two asteroids, one with mass concentrated in the middle, and one with mass concentrated around the edges. (Specifically, the mass distribution follows a spherically symmetric exponential $\rho(r) \propto e^{\pm r^2/a_A^2}$). To prevent the problems seen in previous sections when a symmetric asteroid is simulated,

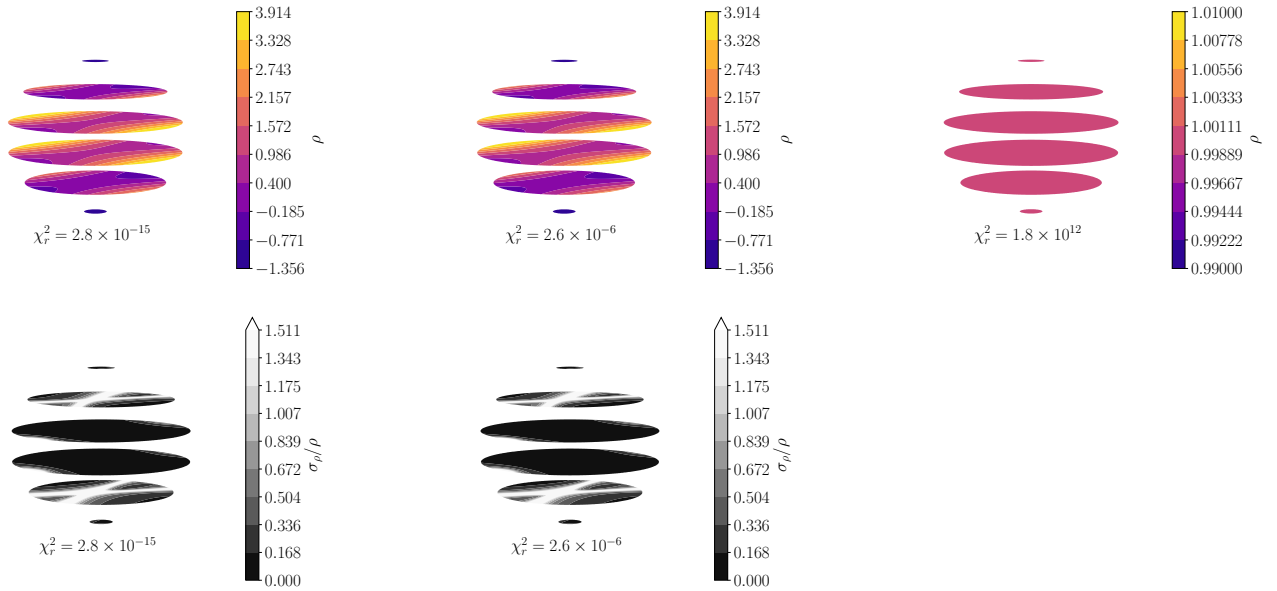


Figure 13. Density distributions extracted by the likelihood (*left*), harmonic (*middle*), and lumpy with $d = N = 1$ (*right*) models from data generated for a uniform-density asymmetric asteroid. The density distributions have been extracted assuming a spherical shape. The extracted density distributions are shown in the top row with uncertainties in the bottom row. Density is normalized so that mean density is one. The same distance scale is used in all figures. Density distributions show clear pathologies when the incorrect shape is used.

we set the shape of the asteroids to the asymmetric reference asteroid. The extracted density distributions are shown in figure 14

For these non-uniform asteroids, the likelihood and harmonic model do not coincide, as can be seen by comparing the density distributions and that χ^2_r is much larger for the harmonic distribution (indicating that the true density distribution is not harmonic). However, the two models give qualitatively similar results in that the centre-weighted density distribution contains more mass in the centre of the asteroid shape for both the harmonic and likelihood models while the edge-weighted asteroid contains mass at the edges. Though these general trends in mass placement arrived at by both the likelihood and harmonic models are accurate, the actual density distributions are inaccurate because they predict negative densities. The difference of the model output from the true distribution is generally less than $1 - 1.5\sigma$ for 95% of the asteroid. However, there are regions with very large uncertainty (as much as 14 times the local density). This leads to deviations from the local density by factors of a much as 4. The locations of these high-uncertainty regions correspond to low-density, in that they occur at the edge of the edge-weighted asteroid and at the center of the center-weighted asteroid.

Figure 14 shows that the lumpy model places one large lump of greater density than the surrounding medium for the centre-weighted asteroid and less density for the edge-weighted asteroid, as expected. Greater error is incurred in χ^2_r in this lumpy model than for the harmonic and likelihood models due to the lumpy model’s crudeness, but the lump gives a good qualitative description of the density distribution of the asteroid which is useful for interpreting the other two models. This fact demonstrates that it can be illustra-

tive to run the models with reduced degrees of freedom for the sake of simplicity, even if doing so yields less accurate distributions.

The lumpy model has one caveat that has not yet been mentioned, which applies for $N = d = 1$ when the density moments are redundant with the asteroid shape; specifically, when (1) the centre of mass of the asteroid is the centroid of the asteroid shape and (2) the density moments of the asteroid shape are proportional to the fitted density moments. (1) guarantees that the lump will be placed at the origin and therefore will not contribute to $K_{\ell m}$ for $\ell \geq 1$, and (2) guarantees that the mass of the asteroid shape will be chosen such that the shape density moments exactly match the fitted density moments. The lump radius will then be set to zero because the fitted density moments are already matched. This zero-radius-lump result will occur even if the true density distribution has a large-radius lump at the origin. The lump model will therefore fail to recognize the lump in the true density distribution.

An example of this caveat applied is an elliptical lump inside an elliptical asteroid similar to the ones above. This is why, in the centre-weighted and edge-weighted density distributions, we specifically chose a spherically symmetric density distribution for our ellipsoidal asteroid shape rather than a distribution that conforms to the asteroid shape.

5 CONCLUSIONS

We derived a novel, arbitrary-order equation for the tidal torque experienced by an asteroid during an encounter with a planet of arbitrary shape and mass distribution. The tidal torque equation (equation 3) revealed that the angular velocity of the asteroid over time depends strongly on $K_{\ell m}$

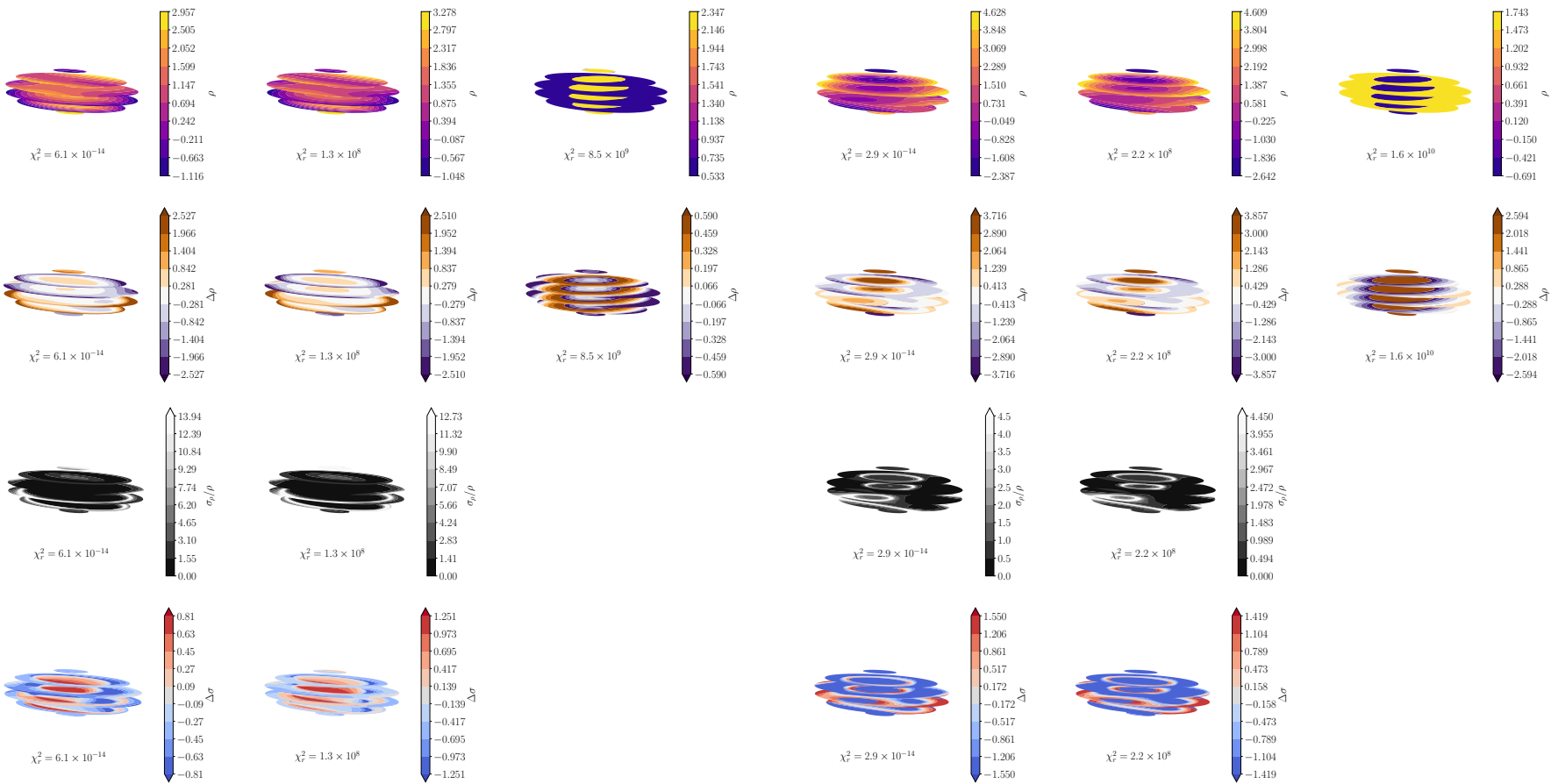


Figure 14. Density distributions extracted for non-uniform-density asteroids with mass concentrated in the middle (left) and the edges (right). Within each half-figure, the likelihood (left), harmonic (middle), and lumpy with $d = N = 1$ (right) models are used. Density is normalized so that mean density is one. The same distance scale is used in all figures. The extracted distributions agree qualitatively with the true distributions, but are highly uncertain and can misestimate the local density by factors of almost 4.

and the initial orientation. We then built a fast simulation for an asteroid encounter, truncating the equation at second-order, and used the simulation to extract first- and second-order density moments from synthetic spin pole data via a Markov Chain Monte Carlo fit. We observe the following general properties of the moments:

- (i) The second-order moments K_{3m} are roughly a factor of $\frac{a_A}{r_p}$ more uncertain than the first-order moments, where a_A is proportional to the asteroid radius and r_p is the perigee distance. For our reference asteroid, this fraction was about 10^{-5} .
- (ii) The second-order moments that measure small-scale variations in density (i.e., $|m|$ is large) are generally less uncertain. It is often possible to measure $K_{3|m|}$ for large m even when K_{30} is not resolved.
- (iii) Extracted density moments are generally more precise when the asteroid leaves the encounter tumbling.
- (iv) The oblateness of the central body cannot be ignored without generating incorrect density moment estimates.

We assessed the posterior uncertainty generated by the fit process by adjusting various properties of an asteroid on an Earth encounter. The precise thresholds we measure (table 1) show that the observational uncertainty and perigee of the asteroid orbit are the most difficult requirements to meet, with perigee $\lesssim 6$ Earth radii, spin pole uncertainty $\lesssim 1^\circ$, and period uncertainty $\lesssim 10$ ms. However, these thresholds depend on the model used to extract a density distribution, and useful information may be able to be extracted when they are not achieved by using a different model.

Finally, we presented three fast, linear methods for extracting density distributions (together with uncertainties) from the density moments and the shape of the asteroid. The extracted density distributions are largely consistent with the true distributions in all cases we tested. Slight adjustments to K_{3m} dramatically change the overall distribution, so that they are not very precise. Indeed, the models sometimes predict negative density (though more complicated models could be made not to). Errors in the shape estimate of the asteroid also distort the density distribution, but the resulting distributions provide hints as to exactly where the shape is incorrect. Large-scale properties of the asteroid's true distribution, such as whether the mass is located in the middle or on the edges, are often observable. Two of the models presented (the harmonic and lumpy models) are flexible in their number of parameters, so that if only these large-scale properties are necessary, a small set of parameters can be chosen to prevent over-fitting.”

ACKNOWLEDGEMENTS

We warmly thank Emmanuel Jehin, Maxime Devogele, and Marin Ferrais for meeting with the authors to discuss this work and pointing out possible future initiatives. JTD also thanks the MIT UROP office for funding his work. This paper made substantial use of MIT Supercloud’s facilities.

DATA AVAILABILITY

The asteroid simulation, fit process, and density moment extraction code are available on [GitHub](#).

REFERENCES

- Ashenberg J., 2007, *Celestial Mechanics and Dynamical Astronomy*, 99, 149
- Baxansky A., Kiryati N., 2007, *Pattern Recognition*, 40, 756
- Benson C. J., Scheeres D. J., Moskovitz N. A., 2020, *Icarus*, 340, 113518
- Berthier J., et al., 2020, *Icarus*, 352, 113990
- Boué G., Laskar J., 2009, *Icarus*, 201, 750
- Brown T., et al., 2013, *Publications of the Astronomical Society of the Pacific*, 125, 1031
- Carroll K., Faber D., 2018, in *Proceedings of the 69th International Astronautical Congress*.
- Descamps P., et al., 2020, *Icarus*, 345, 113726
- Devogèle M., et al., 2021, *Monthly Notices of the Royal Astronomical Society*, 505, 245
- Foreman-Mackey D., Hogg D. W., Lang D., Goodman J., 2013, *Publications of the Astronomical Society of the Pacific*, 125, 306
- Gao F., Han L., 2012, *Computational Optimization and Applications*, 51, 259
- Giorgini J., Benner L., Nolan M., Ostro S., 2005, in *AAS/Division of Dynamical Astronomy Meeting# 36*. pp 02–01
- Giorgini J. D., Benner L. A., Ostro S. J., Nolan M. C., Busch M. W., 2008, *Icarus*, 193, 1
- Hirabayashi M., Kim Y., Brozović M., 2021, *Icarus*, 365, 114493
- Hou X., Scheeres D. J., Xin X., Mar 2017, *Celestial Mechanics and Dynamical Astronomy*, 127, 369
- Kaasalainen M., 2001, *Astronomy & Astrophysics*, 376, 302
- Kaiser N., et al., 2002, in *Survey and Other Telescope Technologies and Discoveries*. pp 154–164
- Larson S., Brownlee J., Hergenrother C., Spahr T., 1998, in *Bulletin of the American Astronomical Society*. p. 1037
- Lee H.-J., et al., 2022.
- Makarov V. V., Goldin A., Tkachenko A. V., Veras D., Noyelles B., 2022.
- Moskovitz N. A., et al., 2020, *Icarus*, 340, 113519
- Naidu S. P., Margot J.-L., 2015, *The Astronomical Journal*, 149, 80
- Pater D. I., Lissauer J. J., 2015, *Planetary sciences*, 2 edn. Cambridge University Press
- Paul M. K., 1988, *Celestial mechanics*, 44, 49
- Pravec P., et al., 2014, *Icarus*, 233, 48
- Richardson D. C., Bottke W. F., Love S. G., 1998, *Icarus*, 134, 47
- Richardson J. E., Melosh H. J., Greenberg R. J., O'Brien D. P., 2005, *Icarus*, 179, 325
- Scheeres D., Ostro S., Werner R., Asphaug E., Hudson R., 2000, *Icarus*, 147, 106
- Scheeres D. J., Marzari F., Rossi A., 2004, *Icarus*, 170, 312
- Smalley K., Garradd G., Benner L., Nolan M., Giorgini J., Chesley S., Ostro S., Scheeres D., 2005, *International Astronomical Union Circular*, 8477, 1
- Souchay J., Souami D., Lhotka C., Puente V., Folgueira M., 2014, *Astronomy & Astrophysics*, 563, A24
- Souchay J., Lhotka C., Heron G., Hervé Y., Puente V., Lopez M. F., 2018, *Astronomy & Astrophysics*, 617, A74
- Stokes G. H., Evans J. B., Viggh H. E., Shelly F. C., Pearce E. C., 2000, *Icarus*, 148, 21
- Tyson J. A., 2002, *Survey and Other Telescope Technologies and Discoveries*, 4836, 10
- Valvano G., Winter O. C., Sfair R., Machado Oliveira R.,

- Borderes-Motta G., Moura T., 2022, Monthly Notices of the Royal Astronomical Society, 510, 95
 Wright E. L., et al., 2010, The Astronomical Journal, 140, 1868
 Yu Y., Richardson D. C., Michel P., Schwartz S. R., Ballouz R.-L., 2014, Icarus, 242, 82
 van Gelderen M., 1998, In the shift operators and translations of spherical harmonics.

APPENDIX A: TIDAL TORQUE & EQUATIONS OF MOTION

In this appendix, we derive the equations of motion used to simulate the asteroid angular velocity during the encounter. In particular, we describe our coordinates (section A1) for an encountering asteroid's position and orientation, and we parametrize its density distribution via its “density moments” (section A2). Then we derive an arbitrary-order equation for tidal torque (section A3) and write the equations of motion for the system (section A4). We do not consider any third-body perturbations, and we assume that the body being encountered (the central body, e.g. a planet) is much more massive than the asteroid.

A1 Coordinates

We make use of two frames of reference to model this system. One is the “inertial frame,” with axes denoted by $\hat{\mathbf{X}}, \hat{\mathbf{Y}}, \hat{\mathbf{Z}}$ and origin placed at the central body’s centre of mass. $\hat{\mathbf{X}}$ points from the central body to the asteroid periape, and $\hat{\mathbf{Z}}$ points parallel to the orbit angular momentum. We assume that the mass distribution of the central body is known in this inertial frame.

Our second frame is the “body-fixed” frame, denoted by $\hat{\mathbf{x}}, \hat{\mathbf{y}}, \hat{\mathbf{z}}$. Each axis in this frame is aligned with a principal axis and rotates with the asteroid, with its origin at the asteroid’s centre of mass. For definiteness, we define $\hat{\mathbf{z}}$ to be the principal axis with maximal moment of inertia (this is the short axis mode, to use the vocabulary of Ref. Kaasalainen (2001)). In general, we use capital letters to denote vectors in the inertial frame and lowercase vectors to denote vectors in the body-fixed frame.

The difference between the origins of the body-fixed and inertial frames is the position of the asteroid. We represent the relative orientations by $z - y - z$ Euler angles α, β , and γ , such that a matrix M rotating from the body-fixed to the inertial frame ($M\mathbf{r} = \mathbf{R}$) is given by

$$M = R_z(\alpha)R_y(\beta)R_z(\gamma). \quad (\text{A1})$$

Here, $R_i(\theta)$ is a rotation around the unit vector i by θ (figure A1).

A2 Density moments

In the next section, it will be shown that only certain parameters of the asteroid density distribution affect tidal torque called “density moments.” First, we define the unnormalized spherical harmonics $Y_{\ell m}(\theta, \phi) = P_{\ell m}(\cos \theta)e^{im\phi}$, where $P_{\ell m}$ are the associated Legendre Polynomials without the Condon-Shortley phase. The regular and irregular

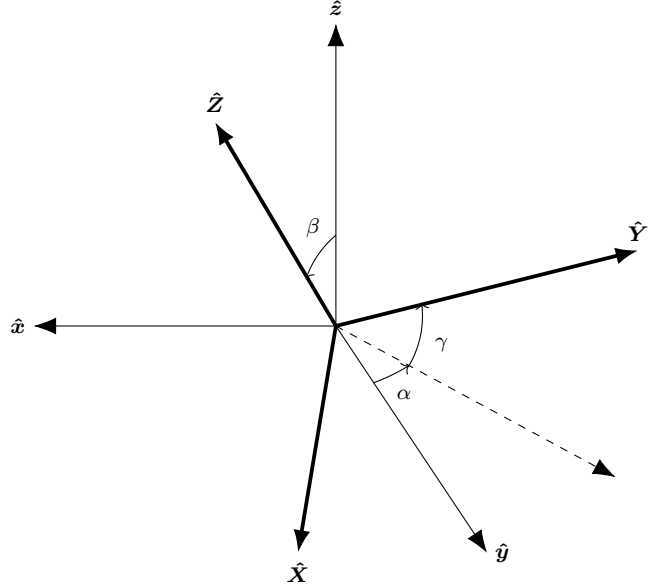


Figure A1. $z - y - z$ Euler angles used in this work to express the orientation of the asteroid. Orientation is expressed as a rotation from the body-fixed axes (lowercase) to the inertial axes (bold and uppercase). The origins are co-located for demonstration purposes.

spherical harmonics then defined as

$$\begin{aligned} S_{\ell m}(\mathbf{r}) &= (-1)^m (\ell - m)! \frac{Y_{\ell m}(\hat{\mathbf{r}})}{r^{\ell+1}} \\ R_{\ell m}(\mathbf{r}) &= (-1)^m \frac{r^\ell}{(\ell + m)!} Y_{\ell m}(\hat{\mathbf{r}}). \end{aligned} \quad (\text{A2})$$

These spherical harmonics obey many useful identities summarized in Ref. van Gelderen (1998), which are also useful for quantum mechanics.

We define the density moments of an asteroid in equation 1. Note that these are complex. The length defined in equation 2 can be thought of as akin to the radius of the asteroid (a spherical, uniform-density asteroid has radius $a_A \sqrt{5/3}$). Both equations 2 and 1 should be computed in the body-fixed frame.

Equations 2 and 1 can be extended to the central body:

$$\begin{aligned} J_{\ell m} &= \frac{1}{\mu_B a_B^\ell} \int_B d^3 r \rho_B(\mathbf{r}) R_{\ell m}(\mathbf{r}) \\ a_B^2 &= \frac{1}{\mu_B} \int_B d^3 r \rho_B(\mathbf{r}) r^2. \end{aligned} \quad (\text{A3})$$

which should be computed in the inertial frame.

Note that both $J_{\ell m}$ and $K_{\ell m}$ are unitless. We call them “moments” because the $R_{\ell m}(\mathbf{r})$ contains an r^ℓ dependence so that $K_{\ell m}$ is the ℓ th density moment of the asteroid. The gravitational potential field of the asteroid can be written entirely in terms of $K_{\ell m}$ and a_A , so we expect not to need any information about the density distribution of the asteroid beyond these parameters to compute tidal torque.

These moments share several key properties which we discuss before continuing. Firstly, for real mass density, properties of the spherical harmonics imply that $K_{\ell m} = (-1)^m K_{\ell, -m}^*$. Therefore, the set of $K_{\ell m}$ for $\ell < \ell_{\max}$ contains ℓ_{\max}^2 degrees of freedom. However, some of these de-

ℓ	$\Re K_{\ell 3}$	$\Im K_{\ell 3}$	$\Re K_{\ell 2}$	$\Im K_{\ell 2}$	$\Re K_{\ell 1}$	$\Im K_{\ell 1}$	$K_{\ell 0}$
0							-
1					x	y	z
2			-	x,y	y,z	x,z	-
3	x,z	y,z	z	x,y,z	x	y	z

Table A1. Axes of mirror symmetry that imply zeroed density moments. For example, for mirror symmetries along \hat{y} or \hat{z} , $\Im K_{32} = 0$. Mirror symmetry along \hat{x} means $\rho_A(x, y, z) = \rho_A(-x, y, z)$. Dashes indicate that none of the mirror symmetries zero the moment in question. Since $r^2 > 0$ for $r \neq 0$, no symmetries set $a_A = 0$ either.

grees of freedom are redundant with the choice of coordinates as we discuss next.

By definition, $K_{00} = 1$. Furthermore, $K_{1m} = 0$ since the body-fixed frame is centred on the asteroid centre of mass. Further calculation reveals that the alignment of the body-fixed frame with the asteroid principal axes also forces $K_{21} = 0$ and $\Im K_{22} = 0$ and the same for $m < 0$. The only physical density moments for $\ell \leq 2$ are therefore K_{22} and K_{20} , which are related to the moment of inertia around each principal axis by equation 4. Incidentally, the definition of a_A was chosen to satisfy equation 4.

The physical meaning of K_{22} and K_{20} can also be interpreted via a special case: if the asteroid is a uniform-density triaxial ellipsoid, the moments of inertia are simple to compute in terms of the semi-axis lengths and can be compared to those found in equation 4. This yields semi-axis lengths of

$$\begin{aligned} a &= \sqrt{\frac{5}{3}} a_A \sqrt{1 - 2K_{20} + 12K_{22}} \\ b &= \sqrt{\frac{5}{3}} a_A \sqrt{1 - 2K_{20} - 12K_{22}} \\ c &= \sqrt{\frac{5}{3}} a_A \sqrt{1 + 4K_{20}}. \end{aligned} \quad (\text{A4})$$

The physical meaning of the higher-order moments K_{3m} can be aided by assessing their symmetry properties. An asteroid that is mirror-symmetric along the \hat{x} axis (meaning $\rho_A(x, y, z) = \rho_A(-x, y, z)$) necessarily sets certain density moments to zero. Which density moments are zeroed by which mirror symmetries is outlined in table A1. Note that, while no mirror symmetries set K_{00} , K_{20} , or K_{22} equal to zero, mirror symmetries exist which zero all the other moments, including K_{3m} . $\Re K_{32}$, K_{31} , and K_{30} are the only K_{3m} components zeroed by only one axis. This will not affect our fit results for K_{3m} , but when we compute density moments for sample distributions, we find that most $K_{3m} = 0$.

Finally, the requirement that $\rho_A(\mathbf{r}) \geq 0$ everywhere restricts $K_{\ell m}$. In the case of K_{2m} , this fact and the constraint that I_z is larger than I_x or I_y requires K_{20} and K_{22} to fall in the triangle

$$-\frac{1}{4} \leq K_{20} \leq 0, \quad |K_{22}| \leq -\frac{K_{20}}{2}. \quad (\text{A5})$$

In practice, we also observe that $|K_{3m}| < 1$; often, $|K_{3m}| < 0.01$ even.

A3 Tidal torque

Derivations for the tidal torque experienced by a rigid body in the gravitational field of a larger mass have been com-

puted by several previous studies Paul (1988); Hou et al. (2017); Boué & Laskar (2009); Ashenberg (2007), often in terms of the moment of inertia of the rigid body (or higher order moments of inertia), and to varying degrees of precision. A simple, first-order derivation is also easily computable in terms of the asteroid moment of inertia in the inertial frame.

Here, we present a novel derivation of the tidal torque to arbitrary orders in terms of the density moments of an asteroid defined in section A2. These density moments can be pre-computed and do not have to be re-evaluated every time-step.

Throughout this paper, we assume that the asteroid remains rigid throughout the encounter. We also assume no third-body perturbations from other Solar System objects. (Actually, third-body perturbing objects are allowed if they are closer to the central body's centre of mass than the asteroid perigee distance. Then, their density moments can be included in the density moments of the central body and this derivation can still be used.) For the sake of simplicity, we also assume that the density moments of the central body are known and do not evolve with time (i.e., the central body's rotation is marginal compared to the timescale of the encounter).

The gravitational potential energy of the central body is, in its most general form,

$$V(\mathbf{R}') = -G \int_{\mathcal{B}} d^3 R \rho_{\mathcal{B}}(\mathbf{R}) \frac{1}{|\mathbf{R} - \mathbf{R}'|}. \quad (\text{A6})$$

where $\rho_{\mathcal{B}}$ is the density distribution of the central body and \mathcal{B} indicates the central body's volume. All vectors here are written in the inertial frame. Given $|\mathbf{R}| < |\mathbf{R}'|$, Ref. van Gelderen (1998) gives the identity

$$\frac{1}{|\mathbf{R} - \mathbf{R}'|} = \sum_{\ell,m} R_{\ell m}(\mathbf{R}) S_{\ell m}^*(\mathbf{R}'), \quad (\text{A7})$$

where the sum is shorthand for $\sum_{\ell,m} = \sum_{\ell=0}^{\infty} \sum_{m=-\ell}^{\ell}$. We are interested in translating the potential energy of equation A6 to the body-fixed frame. To do this, we let $\mathbf{R}' = \mathbf{D} + \mathbf{U}$, where \mathbf{D} is the location of the asteroid in the inertial frame. We further define $\mathbf{U} = M\mathbf{u}$, where \mathbf{u} is in the body-fixed frame and M is the rotation matrix given by the Euler angles α , β , and γ (see section A1). The translation from \mathbf{R}' to \mathbf{U} is then attained by the identity

$$S_{\ell m}(\mathbf{R}') = \sum_{\ell',m'} (-1)^{\ell'} R_{\ell' m'}^*(\mathbf{U}) S_{\ell+\ell',m+m'}(\mathbf{D}), \quad (\text{A8})$$

provided by Ref. van Gelderen (1998), and from \mathbf{U} to \mathbf{u} is given by

$$\begin{aligned} Y_{\ell m}(M\mathbf{u}) &= \sum_{m'=-\ell}^{\ell} (-1)^{m+m'} \sqrt{\frac{(\ell-m')!(\ell+m)!}{(\ell+m')!(\ell-m)!}} \\ &\quad \times \mathcal{D}_{mm'}^{\ell}(M)^* Y_{\ell m'}(\mathbf{u}). \end{aligned} \quad (\text{A9})$$

Here, $\mathcal{D}_{mm'}^{\ell}(M)$ are the Wigner-D matrices, which are determined by the Euler angles α , β , and γ of M .

Equations A6 to A9 then provide formula for $V(\mathbf{u})$ expressed as a sum of integrals over \mathcal{B} of the central body density $\rho_{\mathcal{B}}(\mathbf{R})$ times $R_{\ell m}(\mathbf{R})$. These are expressed via equation A3 as $J_{\ell m}$.

The tidal torque experienced by the asteroid (in the

body-fixed frame) is given by

$$\tau(\mathbf{u}) = \int_{\mathcal{A}} d^3 u \rho_{\mathcal{A}}(\mathbf{u}) (\mathbf{u} \times (-\nabla_{\mathbf{u}} V(\mathbf{u}))) \quad (\text{A10})$$

where $\rho_{\mathcal{A}}$ is the density distribution of the asteroid and \mathcal{A} indicates the volume of the asteroid. Making use of one more identity concerning the derivatives of spherical harmonics:

$$\begin{aligned} \mathbf{u} \times \nabla R_{\ell m}(\mathbf{u}) = & \frac{1}{2} \left[(i\hat{\mathbf{x}} - \hat{\mathbf{y}})(\ell - m + 1)R_{\ell, m-1}(\mathbf{u}) \right. \\ & + (i\hat{\mathbf{x}} + \hat{\mathbf{y}})(\ell + m + 1)R_{\ell, m+1}(\mathbf{u}) \\ & \left. + 2im\hat{\mathbf{z}}R_{\ell m}(\mathbf{u}) \right], \end{aligned} \quad (\text{A11})$$

tidal torque can now be expressed as a function only of $J_{\ell m}$, $K_{\ell m}$, $a_{\mathcal{A}}$, $a_{\mathcal{B}}$, and the asteroid orientation and position. This equation is given explicitly as equation 3. Some $K_{\ell m}$ terms are written in this equation with $|m| > \ell$; these should all be taken to be zero.

Equation 3 possesses a few explicit properties which we discuss before writing the asteroid equations of motion. Firstly, K_{00} does not appear, so that $\boldsymbol{\tau}$ is independent of asteroid mass. The mean density of the asteroid is therefore not constrained by tidal torque analysis. Secondly, torque is largest when D is small (as expected), with the leading order of $\boldsymbol{\tau}$ proportional to D^{-3} . Thirdly, each $J_{\ell m}K_{\ell' m'}$ term is multiplied by $(a_{\mathcal{B}}/D)^{\ell}(a_{\mathcal{A}}/D)^{\ell'}$, the latter of which especially is small in most cases. Equation 3 can therefore be computed approximately by removing terms of large ℓ and ℓ' . For our analysis, we removed $\ell' > 3$ and we usually keep only $\ell = 0$. Note that $\ell = 1$ contributes nothing since $J_{1m} = 0$.

Further insight can be gained by remarking the value of the first-order of $\boldsymbol{\tau}$ for particular Euler angle cases. Setting $\beta = 0$ produces diagonal Wigner- D matrices, and hence $\boldsymbol{\tau} \parallel \hat{\mathbf{z}}$ to first-order. Also, the component τ_z oscillates, so that for certain values of α and γ , $\boldsymbol{\tau} = 0$. This $\beta = 0$ condition is equivalent to $\hat{\mathbf{z}} \parallel \hat{\mathbf{Z}}$ (see figure A1).

For $\beta = \pi/2$, there are two interesting cases. One is for $\alpha = \phi$ (or $\alpha = \pi + \phi$), where ϕ is the angle between the asteroid and the perigee. In this case, $\boldsymbol{\tau} = 0$ to first-order. The second case is $\alpha = \phi \pm \pi/2$, when again $\boldsymbol{\tau} \parallel \hat{\mathbf{z}}$ and τ_z oscillates. At perigee ($\phi = 0$), these conditions are equivalent to $\hat{\mathbf{z}} \parallel \hat{\mathbf{X}}$ and $\hat{\mathbf{z}} \parallel \hat{\mathbf{Y}}$ respectively.

The $\boldsymbol{\tau} \parallel \hat{\mathbf{z}}$ cases are interesting because they do not induce tumbling. If velocity is $\boldsymbol{\omega} \parallel \hat{\mathbf{z}}$ (a non-tumbling state, since $\hat{\mathbf{z}}$ is a principal axis), then $\boldsymbol{\omega} \parallel \mathbf{L}$ and $\boldsymbol{\tau} = \dot{\mathbf{L}} \parallel \dot{\boldsymbol{\omega}}$ so that $\boldsymbol{\omega}$ remains parallel to $\hat{\mathbf{z}}$ and non-tumbling. These cases of torque are additionally significant because not as many terms contribute to τ_z as to τ_x and τ_y .

A4 Equations of motion

The equations of motion of the asteroid position \mathbf{D} are given by Newton's law of gravitation:

$$\dot{\mathbf{V}} = -\frac{G\mu_{\mathcal{B}}}{D^3} \mathbf{D} \quad \dot{\mathbf{D}} = \mathbf{V} \quad (\text{A12})$$

Rather than derive equations of motion for the Euler angles (which suffer from gimbal lock), we instead represent the orientation of the asteroid with a quaternion $\tilde{\mathbf{q}}$ which can be converted into Euler angles to compute $\mathcal{D}(\alpha, \beta, \gamma)$. This

quaternion evolves as

$$\dot{\tilde{\mathbf{q}}} = \frac{1}{2}\tilde{\mathbf{q}}\tilde{\boldsymbol{\omega}}. \quad (\text{A13})$$

for angular velocity $\boldsymbol{\omega}$ given in the body-fixed frame. The equations of motion of $\boldsymbol{\omega}$ in turn are given by

$$\begin{aligned} I_x\dot{\omega}_1 - \omega_y\omega_z(I_y - I_z) &= \tau_x \\ I_y\dot{\omega}_2 - \omega_z\omega_x(I_z - I_x) &= \tau_y \\ I_z\dot{\omega}_3 - \omega_x\omega_y(I_x - I_y) &= \tau_z. \end{aligned} \quad (\text{A14})$$

Equations 3 to A14 form a set of non-linear, first-order coupled differential equations in which can be numerically integrated. They are expressed in terms of the constant physical parameters $\mu_{M/m}$, $a_{M/m}$, $J_{\ell m}$ and $K_{\ell m}$ given the density moment-moment of inertia relations given by equation 4.

Note that equation A14 is independent of $a_{\mathcal{A}}$ to first-order in $\boldsymbol{\tau}$, because $I_j \propto a_{\mathcal{A}}^2$ for all j and $\boldsymbol{\tau} \propto a_{\mathcal{A}}^2$. Therefore, scaling $a_{\mathcal{A}}$ merely scales the value of the sub-leading-order contributions to $\boldsymbol{\tau}$.

APPENDIX B: REFERENCE ASTEROID CONFIGURATIONS

Except when otherwise mentioned, we use the following asteroid encounter parameters. Many of the parameter choices are made to maximize the quality of observations (a close orbit, large asteroid, etc.) This is so that our uncertainties have room to grow; if the reference asteroid has low uncertainty, we would not be able to measure uncertainty increases as well when the encounter parameters are adjusted.

- (i) An orbit around a spherical, Moonless Earth with 6 km s^{-1} excess velocity and perigee at 5 Earth radii. This orbit was chosen to roughly match that of 99942 Apophis [Giorgini et al. \(2005, 2008\)](#); [Smalley et al. \(2005\)](#), discovered on June 19, 2004 by R. A. Tucker, D. J. Tholen, and F. Bernardi. These orbital parameters correspond to an eccentricity of 3.88. The comparison to Apophis is complicated by the fact that Apophis is smaller than our $a_{\mathcal{A}}$ value, is tumbling [Pravec et al. \(2014\)](#), and may change slightly in physical properties due to tidal interaction during the encounter [Yu et al. \(2014\)](#); [Hirabayashi et al. \(2021\)](#). It therefore is not entirely comparable to our analysis.
- (ii) An initial roll of $\gamma_0 = \pi/8$.
- (iii) A cadence of 2 minutes and observational uncertainty of $\sigma_{\theta} = 0.01$ and $\sigma_{\rho}/\sigma_{\theta} = 10^{-5}$.
- (iv) A rotational period of 9 hours, with the angular velocity vector distributed between the $\hat{\mathbf{X}}$, $\hat{\mathbf{Y}}$, and $\hat{\mathbf{Z}}$ axes in a $1 : 2 : -2$ ratio.
- (v) An asteroid with radius $a_{\mathcal{A}} = 1 \text{ km}$ and $K_{3m} = 0$. For K_{22} and K_{20} , we use two standard values: one with $(K_{22}, K_{20}) = (0, -0.097)$ and one with $(0.052, -0.202)$. Including the third point obtained by reflection $K_{22} \rightarrow -K_{22}$, these are the three points that minimize the mean distance between an arbitrary point in the allowed parameter space (equation A5) and these reference values. The first point is called the symmetric case because the corresponding uniform-density-ellipsoid model is rotationally symmetric around $\hat{\mathbf{z}}$. The second case and its reflection are called the asymmetric cases. Values of $(0.052, -0.202)$ have $a < b$ in the ellipsoid model, and the reflected value has $a > b$. If

not specified, we use the $a < b$ case. Specifically, the asymmetric case has $a = 1140$ m, $b = 1839$ m, and $c = 565$ m, while the symmetric case has $a = b = 1411$ m and $c = 1008$ m.

The surface of a spherical asteroid with this rotational period and a_A rotates at 25 cm s^{-1} at the equator. The asymmetric and symmetric ellipsoids have maximum equatorial velocities of 36 cm s^{-1} and 27 cm s^{-1} respectively.

We use the asymmetric ellipsoid in nearly all runs, due to the degeneracy induced in our model when $K_{22} = 0$.

APPENDIX C: ADDITIONAL DENSITY MOMENTS

A finite element model was defined in section 2

APPENDIX D: THE CADENCE CUT-OFF

In section 4.1.4, we noted that posterior uncertainty as a function of observation cadence Δt appears to increase suddenly near $\Delta t \sim T_{\text{cad}} = 30 - 40$ min. In this appendix, we discuss the location of this cadence cut-off as a function of the physical parameters of the asteroid.

In figure D1, we display contour plots of posterior uncertainty $\sigma(K_{\ell m})$ of the fit parameters as a function of both cadence Δt and P_ω (left panel) or the relative orbit speed $t_{\text{spin}}/t_{\text{orbit}}$ (right panel). Both panels show the same sudden increase in posterior uncertainty we named T_{cad} , located around the region where $\sigma_\rho/\rho = 100\%$ and now visible as a function of frequency and relative orbit speed. In all cases, the value of γ_0 was set so that all data points achieve the same value of γ at perigee.

Figure D1 demonstrates that large rotational period produces high T_{cad} . The dependence on P_ω agrees with the fact that large rotational periods for fixed cadence lead to better posterior uncertainty, discussed in section 4.1.7. The figure also demonstrates that for large P_ω , T_{cad} depends less strongly on P_{omega} and may even reverse its dependence such that increasing P_{omega} decreases T_{omega} . In all cases except $\Re K_{33}$, at least constant- $\sigma(K_{\ell m})$ contour is seen to curve back such that Δt decreases as a function of P_{omega} for large P_{omega} . In these regions the cadence cut-off also dulls, as shown by the spreading of the constant- $\sigma(K_{\ell m})$ contours in this region.

The relative orbit speed $t_{\text{spin}}/t_{\text{orbit}}$ was defined by unphysically increasing or decreasing the time at which the asteroid moved through the orbit determined by the equations of motion (but leaving the orbit shape unchanged). The equations of motion affecting the orientation and spin of the asteroid however were unaffected. $t_{\text{spin}}/t_{\text{orbit}} > 1$ corresponds to a faster orbit, and $t_{\text{spin}}/t_{\text{orbit}} < 1$ corresponds to a slower orbit. With this unphysical process, we isolate the effect of the amount of time spent near perigee on posterior uncertainty, without inheriting additional affects that would have been caused by the orbit changing shape.

The right panel of figure D1 shows a stronger and more monotonic dependence of T_{cad} on $t_{\text{spin}}/t_{\text{orbit}}$. It appears that even slightly slower orbits sharply increases T_{cad} . This effect is both due to the asteroid spending greater time in the high-torque, near-perigee region, and the larger data set that can

be collected for slow orbits. However, if the orbit speed is changed by adjusting its parameters (v_∞ , r_p) or the central body mass μ_B , then the orbit shape will also change. This induces other effects studied in the main text and will complicate the trend observed here. Unlike the P_ω case, the cadence cut-off does not visibly broaden as a function of $t_{\text{spin}}/t_{\text{orbit}}$. It appears that the increased orbit speed merely shifts T_{cad} rather than changing its sharpness.

APPENDIX E: COMPUTING ASTEROID SHAPE FROM DENSITY MOMENTS

In section 2.4, we mention that the shape of the asteroid can be computed from observations of the density moments and a_A if a uniform density distribution is assumed. We did not further describe the model in the main text because it is unlike the other three models in the nature of its assumptions, and in the fact that it is non-linear. However, it may be a useful technique so it is mentioned here; we call it the “surface” model. A similar model was also studied in Ref. [Baxansky & Kiryati \(2007\)](#).

Suppose our asteroid has constant density ρ_0 and known parameters $K_{\ell m}$ and a_A^2 , and that the asteroid is “star shaped” in that every ray originating from the centre of mass of the asteroid (the origin of the body-fixed frame) passes through the surface of the asteroid exactly once, at distance $r(\theta, \phi)$ written in spherical coordinates. By the divergence theorem, we write

$$K_{\ell m} = \frac{\rho_0}{\mu_A a_A^\ell} \oint_{\partial A} d^2 \mathbf{r} \cdot \mathbf{v}(\mathbf{r}) \quad (E1)$$

where $\mathbf{v}(\mathbf{r}) = \hat{\mathbf{r}} R_{\ell m}(\mathbf{r}) r / (3 + \ell)$ so that $\nabla \cdot \mathbf{v}(\mathbf{r}) = R_{\ell m}(\mathbf{r})$. The integral is carried out over the surface of the asteroid. We know the area element satisfies $d^2 \mathbf{r} = (\partial \mathbf{r} / \partial \theta \times \partial \mathbf{r} / \partial \phi) d\theta d\phi$ in our coordinates, and when dotted with $\mathbf{v} \parallel \hat{\mathbf{r}}$, this gives

$$K_{\ell m} = \frac{\rho_0}{\mu_A a_A^\ell (3 + \ell)} \int d\Omega r(\theta, \phi)^3 R_{\ell m}(r(\theta, \phi), \theta, \phi). \quad (E2)$$

where the integral is carried out over the unit sphere. Note that the integrand of each $K_{\ell m}$ is proportional to $r(\theta, \phi)^{(3+\ell)}$ times constants and a spherical harmonic.

We write

$$r(\theta, \phi) = \sum_{\ell m} Y_{\ell m}^* C_{\ell m} \quad (E3)$$

without loss of generality. To keep $r(\theta, \phi) \in \mathbb{R}$, we require $C_{\ell m}^* = (-1)^m C_{l, -m}(\ell - m)! / (\ell + m)$. With this definition, equation E2 becomes a polynomial of degree $3 + \ell$ in terms of $C_{\ell m}$ and integrals of products of spherical harmonics. These integrals can be pre-computed so that equation E2 can then be numerically solved via standard polynomial solution methods to find $C_{\ell m}$. A similar equation to equation E2 can be written for a_A

$$a_A^2 = \frac{\rho_0}{5\mu_A} \int d\Omega r(\theta, \phi)^5 \quad (E4)$$

which can also be solved via polynomial methods.

Equations E2 and E4 form $(\ell_{\max} + 1)^2 + 1$ constraints, where ℓ_{\max} is the maximum degree of $C_{\ell m}$. By setting the same maximum degree as for the known $K_{\ell m}$, the system is well-determined and will yield finitely many solutions. These

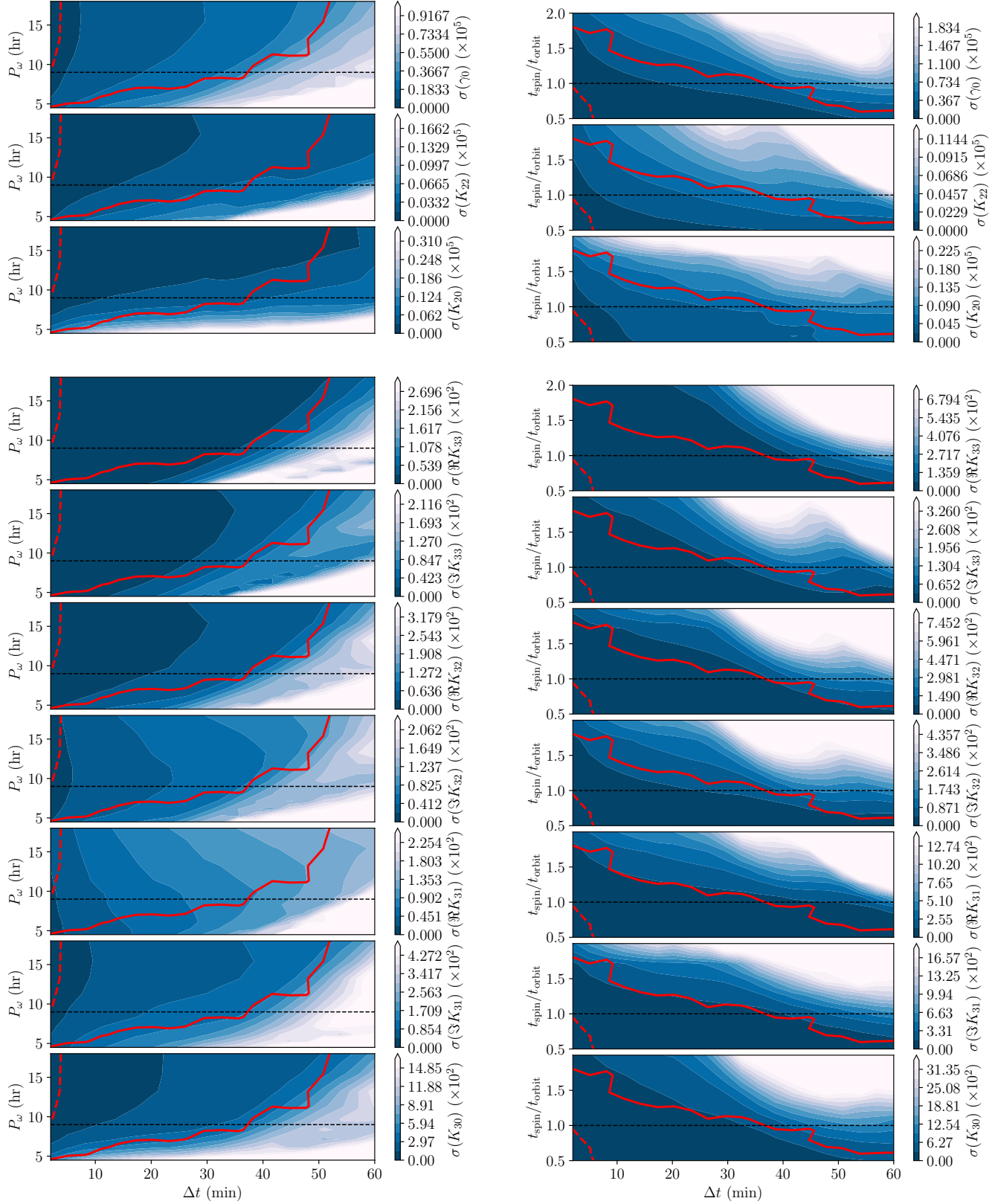


Figure D1. Contour plots showing posterior uncertainties as a function of cadence Δt and dynamical time scales for the encounter: rotational period P_ω (*left*) and the relative speed of the orbit (*right*; see text for a definition). The reference values of $P_\omega = 9$ hr and $t_{\text{spin}}/t_{\text{orbit}} = 1$ are shown as dotted lines. The solid (dotted) red line represents the $\sigma_\rho/\rho = 100\%$ (20%) threshold. Cadence cut-off depends strongly on both P_ω and $t_{\text{spin}}/t_{\text{orbit}} = 1$.



Figure E1. *Left:* the surface of a near-spherical asteroid with uniform density distribution extracted via the surface model. *Right:* the density distribution extracted via the likelihood model for the same density moments but a spherical surface. The same length scale is used in both figures. This new shape model successfully estimates an asteroid shape which is qualitatively consistent with the distributions extracted via models from the main text.

solutions can be filtered by removing those that produce $r(\theta, \phi) < 0$ for any θ, ϕ , which is unphysical.

To test the model, this process was run for an asteroid with $K_{1m} = K_{2m'} = 0$, but randomly chosen K_{3m} in the range 0.01 to -0.01. The resulting surface is shown in figure E1. The figure shows a near-spherical asteroid, which is expected for $K_{\ell m} = 0$ for $\ell > 0$. However, the additional K_{3m} components clearly induce non-sphericity in the asteroid which is captured by the surface model.

To give an alternate view of the non-sphericities found via this new surface model, figure E1 also displays the density distribution extracted via the likelihood model assuming a spherical asteroid shape, but with the same density moments. (Uncertainty in the moments is not modelled in this figure, to better compare the two.) Where the likelihood model displays low density, the surface model clearly retracts into the asteroid. Where the likelihood model yields high density, the surface model extends. Thus, the connection made in section 4.3.1 between non-uniformities in extracted densities at the asteroid surface and inaccuracies in the surface shape is more firmly represented.

This surface model could, in principle, be used to improve estimates of the surface of an asteroid made by light curve analysis, since it connects rotational data to the asteroid surface which reflects the light we observe. Thus, uncertainties either in the density moments or the asteroid surface (or both), could be reduced. However, light-curve analysis is beyond the scope of this paper.

This paper has been typeset from a TeX/LaTeX file prepared by the author.